Geophysical Journal International

Geophys. J. Int. (2017) **209,** 86–105
Advance Access publication 2017 January 13
GJI Geodynamics and tectonics

doi: 10.1093/gji/ggw493

Towards adjoint-based inversion of time-dependent mantle convection with nonlinear viscosity

Dunzhu Li,[1] Michael Gurnis[1] and Georg Stadler[2]

[1]*Seismological Laboratory, California Institute of Technology, Pasadena, CA* 91125, *USA. E-mail: gurnis@gps.caltech.edu*
[2]*Courant Institute of Mathematical Sciences, New York University, NY* 10012, *USA*

Accepted 2017 January 3. Received 2016 December 5; in original form 2016 July 8

SUMMARY

We develop and study an adjoint-based inversion method for the simultaneous recovery of initial temperature conditions and viscosity parameters in time-dependent mantle convection from the current mantle temperature and historic plate motion. Based on a realistic rheological model with temperature-dependent and strain-rate-dependent viscosity, we formulate the inversion as a PDE-constrained optimization problem. The objective functional includes the misfit of surface velocity (plate motion) history, the misfit of the current mantle temperature, and a regularization for the uncertain initial condition. The gradient of this functional with respect to the initial temperature and the uncertain viscosity parameters is computed by solving the adjoint of the mantle convection equations. This gradient is used in a preconditioned quasi-Newton minimization algorithm. We study the prospects and limitations of the inversion, as well as the computational performance of the method using two synthetic problems, a sinking cylinder and a realistic subduction model. The subduction model is characterized by the migration of a ridge toward a trench whereby both plate motions and subduction evolve. The results demonstrate: (1) for known viscosity parameters, the initial temperature can be well recovered, as in previous initial condition-only inversions where the effective viscosity was given; (2) for known initial temperature, viscosity parameters can be recovered accurately, despite the existence of trade-offs due to ill-conditioning; (3) for the joint inversion of initial condition and viscosity parameters, initial condition and effective viscosity can be reasonably recovered, but the high dimension of the parameter space and the resulting ill-posedness may limit recovery of viscosity parameters.

Key words: Inverse theory; Dynamics of lithosphere and mantle.

1 INTRODUCTION

Mantle convection and plate motions are closely coupled (e.g. Davies 1999). The constitutive relation (viscosity law) plays a first-order role in determining not only the extent of this coupling but also the structure and evolution of mantle convection. Despite substantial effort attempting to determine the viscosity structure of the mantle, either through forward and inverse geophysical models or through laboratory work, many first-order questions remain. For example, while global geophysical flow models have suggested that the strength of lateral viscosity variations might be small (about an order of magnitude) (e.g. Moucha *et al.* 2007; Yang & Gurnis 2016), global forward (Stadler *et al.* 2010) and local inverse models (Baumann & Kaus 2015) suggest that the lateral variations in viscosity associated with plate tectonics may be several orders of magnitude ($>10^3$). In addition, as long evident through forward models (McKenzie *et al.* 1974; Lenardic *et al.* 2003) or plate tectonic reconstructions (see review by Seton *et al.* 2012), mantle convection is highly time-dependent. This time-dependence implies that it is essential to find ways to constrain the structure of mantle convection sequentially backwards in time. Some progress along these lines has been made with global forward models (e.g. Bunge *et al.* 1998; Bower *et al.* 2015) and inverse models (e.g. Bunge *et al.* 2003; Spasojevic *et al.* 2009; Moucha & Forte 2011). Although there has been some attempt to use variable viscosity in such inverse models meant to recover mantle structure in the past (Liu *et al.* 2008), they have not, arguably, approached the realistic variations in viscosity that are critical to the dynamics.

Computational models of mantle convection, often with realistic rheologies, are now commonly used to interpret a wide range of phenomena, such as plate motions, rifting, subduction, basin formation, continental delamination and sea level change. Forward models in particular have become detailed and realistic. For example, a wide range of studies have focused on the time dependence of subduction showing the evolution of slabs (Billen & Hirth 2007; Burkett & Billen 2009; Gerya 2011; Garel *et al.* 2014). Such models show potentially

diagnostic time-dependent phenomena, including how slab structure, including slab dip and the degree of slab folding, change with time. Many of the same classes of phenomena are now found in different studies while qualitatively fitting the general characteristics of plate motions and seismic images of subducted slabs. Given the success with forward models and the general consensus of the classes of phenomena seen in forward models (see reviews by Billen 2008; Gerya 2011), we demonstrate here that these problems can be cast in an inverse sense.

Inverse models for convection have been formulated previously. For example, Bunge *et al.* (2003) proposed an adjoint method to recover an initial condition using seismic 'images' as data, where the mantle flow model uses the plate motion history as boundary conditions. Horbach *et al.* (2014) further derived this initial condition inversion using a general operator formulation, and found that a strong global minimum exists for the unknown initial condition, regardless of the starting model. Ismail-Zadeh *et al.* (2004) also derive an initial condition for the convection problem with an adjoint method while considering a strongly temperature-dependent media. In these studies, the viscosity structure or viscosity parameters are assumed, and did not depend on other state variables such as temperature and strain rate. Liu & Gurnis (2008) proposed an inversion of both viscosity parameters and initial conditions using an embedded pair of loops, where an inner loop with an adjoint of the energy equation, as in Bunge *et al.* (2003), recovers the initial condition assuming known viscosity parameters, while an outer loop recovers the viscosity parameters using a linear least squares formulation for fitting the dynamic topography. The method has been applied to the recovery of subduction history in North America since the Late Cretaceous (Spasojevic *et al.* 2009). Although the viscosity in their model is temperature-dependent, they do not incorporate this dependence in the derivation of the adjoint equation, resulting in an inexact gradient. Our study is similar to these previous studies in terms of the inversion setup, but with several key extensions. We build on the work of Bunge *et al.* (2003), Spasojevic *et al.* (2009), and Horbach *et al.* (2014), and argue that besides initial conditions, a key component of a formal inversion should be the inference of material properties, involving the scaling between seismic velocity anomalies and density and temperature, the parameters that determine the temperature-dependence of viscosity, yield stress, and the nonlinear exponent for strain-rate-dependent viscosity, and so on. The constitutive properties are important because they determine the time-dependent dynamics of subduction and mantle convection (Zhong & Gurnis 1995a; Garel *et al.* 2014). This joint inversion is similar to Liu & Gurnis (2008), but we derive a full adjoint set of equations considering all the dependencies.

The inference of parameters in the rheology is mathematically and algorithmically involved. Worthen *et al.* (2014) studied inversion of such parameters in instantaneous Stokes flow by fitting surface velocity observations, where the temperature structure is assumed given. They invert for spatially varying parameter fields, like pre-factor and nonlinear exponent to the viscosity law, using a limited memory Broyden–Fletcher–Goldfarb–Shanno (BFGS) quasi-Newton method, and find a strong trade-off between the pre-factor and nonlinear exponent fields, although the effective viscosity and viscous dissipation are well recoverable. Following this approach, Ratnaswamy *et al.* (2015) also use an adjoint of the Stokes equation but cast the problem within a Bayesian framework to infer several important viscosity parameters controlling plate coupling, including a yield stress, a nonlinear exponent in the stress-strain rate relation, and a pre-factor for the viscosity, which models individual fault zones. Their unknowns are a small number of scalar parameters rather than parameter fields, which allowed them to solve the Bayesian inverse problem using sampling or to compute a Hessian-based approximation of the posterior parameter distribution. This provides insight into trade-offs between parameters and shows how strongly the data constrain the parameters.

Building on these previous studies, we attempt to solve an inversion problem where the unknowns include both the initial temperature condition and scalar viscosity parameters of the mantle. The data we use are the present-day mantle temperature (which would be inferred from seismic tomography) and the plate reconstruction history. Following a PDE-constrained optimization framework, we define an objective function, compute its gradient using the adjoint method, and solve the optimization problem using a gradient-based method. We illustrate and study our method using two synthetic 2-D examples, a model of a sinking cylinder, and a subduction problem that involves plate motions and uses a realistic viscosity law.

2 GOVERNING EQUATIONS

We study mantle convection and plate motion as governed by a creeping viscous fluid in a Cartesian domain Ω (assumed to be 2-D). Under the Boussinesq approximation for an incompressible fluid, the non-dimensional equations governing mantle convection are the equations for conservation of mass and momentum,

$$\nabla \cdot \boldsymbol{u} = 0, \tag{1a}$$

$$-\nabla \cdot \boldsymbol{\sigma} = \mathrm{Ra} T \boldsymbol{e}_z, \tag{1b}$$

and the equation for conservation of energy

$$\frac{\partial T}{\partial t} + \boldsymbol{u} \cdot \nabla T - \nabla^2 T = 0, \tag{2}$$

where $\boldsymbol{u}$ is the velocity, T the temperature, Ra the Rayleigh number, and $\boldsymbol{e}_z$ the unit vector pointing in the direction of gravity. The stress tensor, $\boldsymbol{\sigma}$, is defined as

$$\boldsymbol{\sigma} = -pI + 2\eta_{\mathrm{eff}} D(\boldsymbol{u}),$$

$$D(\boldsymbol{u}) = \frac{1}{2}\left(\nabla \boldsymbol{u} + (\nabla \boldsymbol{u})^{\mathsf{T}}\right),$$

with p the pressure, and η_{eff} the effective viscosity, which depends on location, temperature and strain rate (details are given below).

We assume Dirichlet conditions for the temperature on the top and bottom of the domain Γ_d, and no-flux conditions on the remaining (side) boundaries, that is,

$$T|_{\Gamma_d} = T_d,$$
$$\nabla T \cdot \boldsymbol{n}|_{\partial\Omega\setminus\Gamma_d} = 0,$$

where $\boldsymbol{n}$ is the unit normal at the boundary, and T_d is the Dirichlet boundary temperature data. For the Stokes equation, we assume a free-slip mechanical condition on all boundaries, that is,

$$\boldsymbol{u} \cdot \boldsymbol{n}|_{\partial\Omega} = 0,$$
$$\boldsymbol{n} \times (\boldsymbol{n} \times \boldsymbol{\sigma}\boldsymbol{n})|_{\partial\Omega} = 0.$$

The initial condition for the temperature is specified as $T_{\text{init}}(\boldsymbol{x})$, that is,

$$T(\boldsymbol{x}, t = 0) = T_{\text{init}}(\boldsymbol{x}).$$

The viscosity of the mantle is governed by the high-temperature creep of silicates, for which laboratory experiments show that the creep strength is temperature-, pressure-, compositional- and stress-dependent (Ranalli & Karato 1995). The effective viscosity η_{eff} is thus specified by the viscosity law

$$\eta_{\text{eff}} = \eta_{\min} + \min\left(\frac{\sigma_{\text{yield}}}{2\sqrt{\varepsilon_{\text{II}}}}, \omega \min(\eta_{\max}, \eta)\right),$$
$$\text{with } \varepsilon_{\text{II}} = \frac{1}{2} D(\boldsymbol{u}) : D(\boldsymbol{u}),\ \eta = C e^{E(0.5-T)} (\varepsilon_{\text{II}})^{\frac{1-n}{2n}}. \tag{3}$$

Here, ε_{II} is the second invariant of the strain rate tensor, $C > 0$ is a viscosity pre-factor, $E > 0$ is the non-dimensional activation energy, $n > 0$ is the nonlinear exponent, $\eta_{\min}$, $\eta_{\max}$ act as minimum and maximum bounds for the effective viscosity, and $\sigma_{\text{yield}} > 0$ is the yield stress. Moreover, we refer to $\omega = \omega(\boldsymbol{x})$, $0 < \omega(\boldsymbol{x}) \leq 1$, as the weakening factor, which is used to incorporate phenomenological aspects that cannot be represented in a purely viscous flow model, such as processes which govern mega-thrust faults along the subduction interface, or partial melting near a mid-ocean ridge. For example, mega-thrust faults are represented using a weakzone stencil (that is, a stencil outlining the region around a mega-thrust thought to have weakened over geological time), where $\omega(\boldsymbol{x}) = 1$ throughout most of the domain, except along the subduction interface and near ridges where $\omega(\boldsymbol{x}) \ll 1$ (and we choose a weakening factor that is smooth throughout the domain). One can allow the stencil to move during the simulation, that is, $\omega = \omega(\boldsymbol{x}, t)$, to model trench rollback/advance, but we currently have not incorporated such a time-dependent stencil in our inversions.

3 DISCRETIZATION

The finite element method (FEM) is widely used for mantle convection computations (e.g. Moresi *et al.* 2000). It is able to accommodate many aspects important to mantle convection, such as complicated geometry, different boundary conditions, variable material properties, and mesh refinement. We build our FE implementation using the deal.II finite element library (Bangerth *et al.* 2007), upon which ASPECT (Kronbichler *et al.* 2012), a community code for mantle convection, is also based. An attractive feature of deal.II is its extensive support for adaptive mesh refinement (AMR) through the p4est library (Burstedde *et al.* 2011). AMR does not require complete specification of the mesh *a priori*, since the mesh can be refined or coarsened according to user-defined error indicators (Kronbichler *et al.* 2012), or according to local temperature gradients or strain rates, or combinations thereof (Burstedde *et al.* 2013). This versatility achieves sufficiently fine local mesh resolution to explore different weak zone descriptions, which play an important role in models of subduction evolution.

The finite element method (Hughes 1987) uses the weak form of eqs (1) and (2) and approximates them in finite dimensions. Here, we describe the resulting finite-dimensional (nonlinear) equations, and highlight the inter-dependence of variables. Our discretization uses Taylor–Hood elements, that is, bi-quadratic elements to approximate temperature and velocity, and bi-linear elements for the pressure. After discretization in space, we discretize in time. We consider the time steps $t^0 < t^1 < \ldots < t^{n_F}$ and denote the discrete temperature, velocity and pressure vectors corresponding to a time t^n by $\mathbf{T}^n$, $\mathbf{u}^n$, and $\mathbf{p}^n$, respectively. For a given $\mathbf{T}^n$, discretization of the nonlinear incompressible Stokes eq. (1) results in the nonlinear system

$$\begin{bmatrix} A^n & B \\ B^T & 0 \end{bmatrix} \begin{bmatrix} \mathbf{u}^n \\ \mathbf{p}^n \end{bmatrix} = \begin{bmatrix} F\mathbf{T}^n \\ \mathbf{0} \end{bmatrix}, \tag{4}$$

where $\mathbf{m}$ are the rheological parameters, $A^n = A(\mathbf{u}^n, \mathbf{T}^n, \mathbf{m})$, and

$$A_i^n = \int 2\eta_{\text{eff}}(\mathbf{u}^n, \mathbf{T}^n, \mathbf{m}) D(\phi_i^{\boldsymbol{u}}) : D\left(\phi_j^{\boldsymbol{u}}\right) \mathrm{d}\Omega,$$

$$B_{ij} = \int -\left(\nabla \cdot \phi_i^{\boldsymbol{u}}\right) \phi_j^p \mathrm{d}\Omega,$$

$$F_{ij} = \int R_a \phi_i^{\boldsymbol{u}} \cdot \left(\phi_j^{\text{temp}} \boldsymbol{e}_z\right) \mathrm{d}\Omega,$$

with $\phi_i^{\boldsymbol{u}} = (\phi_i^{u_1}, \phi_i^{u_2})^\intercal, \phi_i^p, \phi_i^{\text{temp}}$ are the shape functions for the velocity components u_1 and u_2, for the pressure, and the temperature, respectively. We refer to A^n as the stress block, which depends on velocity, temperature and the parameters $\mathbf{m}$, all of which enter in the viscosity. Moreover, we refer to B as the gradient operator.

The energy eq. (2) has the weak form

$$\int \left[\phi \left(\frac{\partial T}{\partial t} + \boldsymbol{u} \cdot \nabla T\right) + \nabla\phi \nabla T\right] \mathrm{d}\Omega = 0,$$

where ϕ is the temperature test function. It is well known that the Galerkin discretization of this weak form of the equation can result in artefacts in the solution of advection-dominated equations such as eq. (2). Several methods exist to control these artefacts, for example, a streamline upwind Petrov-Galerkin (SUPG) formulation (Brooks & Hughes 1982), or an artificial diffusion method as used in ASPECT (Kronbichler *et al.* 2012). Here, we use the SUPG method following (Zhong *et al.* 2007), that is, we change the temperature test function from ϕ to $\phi + \tau \boldsymbol{u} \cdot \nabla\phi$, where τ is the SUPG parameter, which is

$$\tau = \left(\sum_i \tilde{\xi}_i u_i h_i\right) / 2|\boldsymbol{u}|^2 \tag{5}$$

where

$$\tilde{\xi}_i = \begin{cases} -1 - 1/\text{Pe}_i & \text{Pe}_i < -1, \\ 0, & -1 \le \text{Pe}_i \le 1, \\ 1 - 1/\text{Pe}_i, & \text{Pe}_i > 1. \end{cases} \tag{6}$$

Here, $\text{Pe}_i = u_i h_i / 2\kappa$, h_i is the element size in the ith dimension, and κ is the thermal diffusion. This results in the Petrov-Galerkin weak form

$$\int \left[(\phi + \tau \boldsymbol{u} \cdot \nabla\phi)\left(\frac{\partial T}{\partial t} + \boldsymbol{u} \cdot \nabla T\right) + \nabla\phi \nabla T\right] \mathrm{d}\Omega = 0,$$

which expands to

$$\int \left[\phi \frac{\partial T}{\partial t} + (\tau \boldsymbol{u} \cdot \nabla\phi) \frac{\partial T}{\partial t} + \phi \boldsymbol{u} \cdot \nabla T + (\tau \boldsymbol{u} \cdot \nabla\phi)(\boldsymbol{u} \cdot \nabla T) + \nabla\phi \nabla T\right] \mathrm{d}\Omega = 0.$$

Using a finite element discretization in space for T and ϕ, this results in the following system of ordinary differential equations

$$M \frac{\mathrm{d}\mathbf{T}}{\mathrm{d}t} + M^S(\boldsymbol{u}) \frac{\mathrm{d}\mathbf{T}}{\mathrm{d}t} + C(\boldsymbol{u})\mathbf{T} + C^S(\boldsymbol{u})\mathbf{T} + K\mathbf{T} = 0, \tag{7}$$

where

$$M_{ij} = \int \phi_i^{\text{temp}} \phi_j^{\text{temp}} \mathrm{d}\Omega,$$

$$M_{ij}^S = \int \tau \left(\boldsymbol{u} \cdot \nabla\phi_i^{\text{temp}}\right) \phi_j^{\text{temp}} \mathrm{d}\Omega,$$

$$C_{ij} = \int \phi_i^{\text{temp}} \boldsymbol{u} \cdot \nabla\phi_j^{\text{temp}} \mathrm{d}\Omega,$$

$$C_{ij}^S = \int \tau \left(\boldsymbol{u} \cdot \nabla\phi_i^{\text{temp}}\right)\left(\boldsymbol{u} \cdot \nabla\phi_j^{\text{temp}}\right) \mathrm{d}\Omega,$$

$$K_{ij} = \int \nabla\phi_i \cdot \nabla\phi_j \mathrm{d}\Omega.$$

In the above expressions, we considered the velocity function $\boldsymbol{u}$ as given. In practice, $\boldsymbol{u}$ is the discrete velocity function obtained from solving the discretized Stokes problem and we will use the notation $M^S(\mathbf{u})$, $C(\mathbf{u})$ and $C^S(\mathbf{u})$, where $\mathbf{u}$ is the coefficient vector corresponding to the finite element discretization of $\boldsymbol{u}$.

For the time discretization of eq. (7), we employ a second-order implicit method. Kronbichler *et al.* (2012) use a second-order implicit/explicit scheme within the ASPECT code, which requires states from two previous time steps to calculate the next time step. For our inversion problem, we prefer an implicit Runge–Kutta method that only requires the states at one previous time step. Since implicit schemes

are unconditionally stable, we can use the same time steps during the whole inversion process, independent from the convecting velocity. We modify the Runge–Kutta scheme from Bonito *et al.* (2014), that is, to march forward from t^n to t^{n+1}, we introduce the intermediate time step $t^{n+1/2} := t^n + \frac{1}{2}\Delta t^n$, where $\Delta t^n = t^{n+1} - t^n$, and derive the corresponding temperature $\mathbf{T}^{n+1/2}$ from

$$M\frac{\mathbf{T}^{n+1/2} - \mathbf{T}^n}{t^{n+1/2} - t^n} + C(\mathbf{u}^n)\mathbf{T}^n + K\mathbf{T}^{n+1/2} = \mathbf{0}, \tag{8}$$

where $\mathbf{u}^n$ is obtained through the solution of eq. (4). Note that for this half time step, we do not use SUPG stabilization, and the convection term $C(\mathbf{u}^n)\mathbf{T}^n$ is treated explicitly, while the diffusion term $K\mathbf{T}^{n+1/2}$ is treated implicitly. Then, we solve the nonlinear Stokes equation to obtain $\mathbf{u}^{n+1/2}$, $\mathbf{p}^{n+1/2}$ from $\mathbf{T}^{n+1/2}$,

$$\begin{bmatrix} A^{n+1/2} & B \\ B^\mathsf{T} & 0 \end{bmatrix} \begin{bmatrix} \mathbf{u}^{n+1/2} \\ \mathbf{p}^{n+1/2} \end{bmatrix} = \begin{bmatrix} F\mathbf{T}^{n+1/2} \\ \mathbf{0} \end{bmatrix}, \tag{9}$$

where $A^{n+1/2} = A(\mathbf{u}^{n+1/2}, \mathbf{T}^{n+1/2}, \mathbf{m})$. Finally, a full time step is performed, which includes SUPG regularization, and implicit convection and diffusion terms:

$$M\frac{\mathbf{T}^{n+1} - \mathbf{T}^n}{t^{n+1} - t^n} + M^S\left(\mathbf{u}^{n+1/2}\right)\frac{\mathbf{T}^{n+1} - \mathbf{T}^n}{t^{n+1} - t^n} + C\left(\mathbf{u}^{n+1/2}\right)\mathbf{T}^{n+1} + C^S\left(\mathbf{u}^{n+1/2}\right)\mathbf{T}^{n+1} + K\mathbf{T}^{n+1} = \mathbf{0}. \tag{10}$$

To summarize, the forward model eqs (4)–(10) can be written as:

(i) Set $\mathbf{T}^0 = \mathbf{T}_{\text{init}}$.

(ii) Solve, for $n = 0, 1, \ldots, n_F - 1$:

$$\begin{bmatrix} A^n & B \\ B^\mathsf{T} & 0 \end{bmatrix} \begin{bmatrix} \mathbf{u}^n \\ \mathbf{p}^n \end{bmatrix} = \begin{bmatrix} F\mathbf{T}^n \\ \mathbf{0} \end{bmatrix}, \tag{11a}$$

$$M_a^n \mathbf{T}^{n+1/2} = M_b^n \mathbf{T}^n, \tag{11b}$$

$$\begin{bmatrix} A^{n+1/2} & B \\ B^\mathsf{T} & 0 \end{bmatrix} \begin{bmatrix} \mathbf{u}^{n+1/2} \\ \mathbf{p}^{n+1/2} \end{bmatrix} = \begin{bmatrix} F\mathbf{T}^{n+1/2} \\ \mathbf{0} \end{bmatrix}, \tag{11c}$$

$$M_c^{n+1/2} \mathbf{T}^{n+1} = M_d^{n+1/2} \mathbf{T}^n, \tag{11d}$$

where

$$M_a^n = \left(M + \frac{1}{2}\Delta t^n K\right),$$

$$M_b^n = \left(M - \frac{1}{2}\Delta t^n C(\mathbf{u}^n)\right),$$

$$M_c^{n+1/2} = M + M^S\left(\mathbf{u}^{n+1/2}\right) + \Delta t^n\left[K + C\left(\mathbf{u}^{n+1/2}\right) + C^S\left(\mathbf{u}^{n+1/2}\right)\right],$$

$$M_d^{n+1/2} = M + M^S\left(\mathbf{u}^{n+1/2}\right).$$

(iii) Finally, solve eq. (11a) for $n = n_F$ to compute the final time velocity $\mathbf{u}^{n_F}$.

Note that eqs (11a) and (11c) are nonlinear Stokes systems, while the temperature update steps eqs (11b) and (11d) are linear. In our implementation, the nonlinear Stokes system is solved using Newton's method (Ratnaswamy *et al.* 2015). For the 2-D tests shown below, a direct solver is used for the linear systems.

Our numerical tests indicate that the above scheme is stable even for time steps that are orders of magnitude larger than was possible for an explicit scheme. Comparison with previous benchmark results (Blankenbach *et al.* 1989; Travis *et al.* 1990) show its accuracy. For example, for the time-dependent convection problem of a basally heated Rayleigh–Benard convection model in a 2-by-1 domain, with a Rayleigh number of 10^5 and constant viscosity, we find a difference of less than 0.3 per cent compared to the values in table 5 of Travis *et al.* (1990).

4 INVERSE MANTLE CONVECTION

Substantial uncertainties exist with respect to current and past conditions and properties of the mantle. The mantle temperature distribution in the past (treated as initial conditions in our model) and rheological parameters are arguably among the most uncertain. We use an inverse problem approach to study the ability and limitations of reconstructing initial conditions and rheological parameters from present-day temperature data and historic plate motions. This inverse problem is formulated as an optimization problems that is governed by the equations for mantle convection presented in Section 2, or their discretized version presented in Section 3. We follow a 'discretize-then-optimize'

approach, that is, we state the optimization objective and the governing equations in their discretized form, and compute derivatives with respect to the inversion parameters—which are required in the optimization procedure—using this discretized PDE-constrained optimization problem. As discussed, for example, in Giles & Pierce (2000) and Gunzburger (2003), this approach ensures that optimization methods can converge fully, since we compute the exact derivatives of the discrete objective function and thus objective and derivatives are consistent. Additionally, the approach allows one to verify the derivative and its implementation using finite differences, as shown below.

We define the discrete objective function as

$$\begin{aligned}\mathcal{J}(\mathbf{T}_{\text{init}}, \mathbf{m}, \bar{\mathbf{T}}, \bar{\mathbf{u}}) &= \mathcal{J}_F(\mathbf{T}^{n_F}) + \mathcal{J}_S(\bar{\mathbf{u}}) + \mathcal{J}_R(\mathbf{T}_{\text{init}}) \\ &= \frac{\beta_F}{2}(\mathbf{T}^{n_F} - \mathbf{T}_{\text{obs}})^\intercal M(\mathbf{T}^{n_F} - \mathbf{T}_{\text{obs}}) + \frac{\beta_S}{2}\sum_{n=0}^{n_F}\left(O\mathbf{u}^n - \mathbf{u}^n_{\text{obs}}\right)^\intercal\left(O\mathbf{u}^n - \mathbf{u}^n_{\text{obs}}\right) \\ &\quad + \frac{\beta_R}{2}\left(\mathbf{T}_{\text{init}} - \mathbf{T}_{\text{mean}}\right)^\intercal K\left(\mathbf{T}_{\text{init}} - \mathbf{T}_{\text{mean}}\right),\end{aligned} \tag{12}$$

where $\bar{\mathbf{T}} = [\mathbf{T}^0, \ldots, \mathbf{T}^{n_F}]$ and $\bar{\mathbf{u}} = [\mathbf{u}^0, \ldots, \mathbf{u}^{n_F}]$ are the temperature and velocities for all time steps, which depend on $\mathbf{m}$ through the solution of the forward eq. (11). Moreover, $\mathcal{J}_F(\cdot)$, $\mathcal{J}_S(\cdot)$, and $\mathcal{J}_R(\cdot)$ denote the final temperature misfit, the surface velocity misfit, and the initial temperature regularization, respectively, and β_F, β_S, $\beta_R > 0$ are regularization parameters that control the relative weight of the different terms in $\mathcal{J}(\cdot)$. Moreover, M is the mass matrix, and the matrix O denotes an operator that extracts surface velocities from the full velocity field.

The regularization term for the initial temperature field includes an initial condition estimate, $\mathbf{T}_{\text{mean}}$, and the stiffness matrix K, which expresses our preference for smooth initial conditions. Other, non-quadratic regularization that allow discontinuities in the recovered initial field could be used. The final time temperature observation data are $\mathbf{T}_{\text{obs}}$, and $\mathbf{u}^n_{\text{obs}}$ for $n = 0, \ldots, n_F$ are surface velocity observations for all time steps. In this study, these data are synthesized from forward models with known initial time and rheology parameters as described below. In applications with geophysical data, they will come from plate tectonics reconstructions and from seismic (tomographic) images, converted from wave speed to temperature. Note that in this formulation, we assume a constant time step Δt, and the time integration in the surface misfit is replaced with a summation, with Δt absorbed into β_S. Since the three terms occurring in the objective have different units and magnitudes, we consider them to be normalized, that is, in practice we specify a new set of parameters α_F, α_S, α_R and then derive the regularization parameters β_S, β_F, β_R as follows:

$$\beta_S = \frac{\alpha_S}{\frac{1}{2}\sum_{n=0}^{n_F-1}\left(\mathbf{u}^n_{\text{obs}}\right)^2},$$

$$\beta_F = \frac{\alpha_F}{\frac{1}{2}\left(\mathbf{T}_{\text{obs}} - \mathbf{T}_{\text{mean}}\right)^\intercal M\left(\mathbf{T}_{\text{obs}} - \mathbf{T}_{\text{mean}}\right)},$$

$$\beta_R = \frac{\alpha_R}{\frac{1}{2}\left(\mathbf{T}_{\text{obs}} - \mathbf{T}_{\text{mean}}\right)^\intercal K\left(\mathbf{T}_{\text{obs}} - \mathbf{T}_{\text{mean}}\right)}.$$

The objective $\mathcal{J}(\cdot)$ is minimized over the uncertain parameters—the initial temperature $\mathbf{T}_{\text{init}}$ and the viscosity parameters $\mathbf{m}$. For each choice of these parameters, $\bar{\mathbf{T}}$, $\bar{\mathbf{u}}$ must be computed by solving the forward model eq. (11). Thus, this is a PDE-constrained optimization problem, where the PDEs are the mantle flow equations (or their discretization, since we follow the discretize-then-optimize approach). It is common to eliminate the PDE-constraints by considering the temperature and velocity as functions of the parameters $(\mathbf{T}_{\text{init}}, \mathbf{m})$ through the solution of the mantle convection equations. That is, $\bar{\mathbf{T}} = \bar{\mathbf{T}}(\mathbf{T}_{\text{init}}, \mathbf{m})$ and $\bar{\mathbf{u}} = \bar{\mathbf{u}}(\mathbf{T}_{\text{init}}, \mathbf{m})$, and the—now formally unconstrained—minimization problem becomes

$$\min_{\mathbf{T}_{\text{init}}, \mathbf{m}} \hat{\mathcal{J}}(\mathbf{T}_{\text{init}}, \mathbf{m}) := \mathcal{J}(\mathbf{T}_{\text{init}}, \mathbf{m}, \bar{\mathbf{T}}(\mathbf{T}_{\text{init}}, \mathbf{m}), \bar{\mathbf{u}}(\mathbf{T}_{\text{init}}, \mathbf{m})). \tag{13}$$

For this—sometimes called reduced—objective functional, we next derive derivatives with respect to the parameters. These derivatives must take into account the dependence of the temperature and velocity on the parameters, which is given through the solution of the mantle flow equations. The adjoint method (Gunzburger 2003; Tröltzsch 2010; Borzì & Schulz 2012) represents an efficient way to derive expressions for the derivatives of $\hat{\mathcal{J}}$, which are required in a gradient-based descent algorithm to solve eq. (13). Note that this optimization problem can incorporate other constraints, such as bounds on parameters. An alternative approach to imposing bounds is to ensure positivity of parameters such as the viscosity pre-factor C through a reparametrization, for example, we use $\bar{C} = \ln(C)$ rather than C as the parameter in our inversion.

In the numerical examples presented in Sections 8 and 9, we use synthetically generated data for our inversion tests, which aim at studying properties of the inverse problem as well as the performance of the proposed algorithms. These synthetic data are generated by choosing an initial temperature and rheology parameters, solving the discretized forward mantle convection eq. (11), and extracting the synthetic surface velocity data $\mathbf{u}^n_{\text{obs}} = O\mathbf{u}^n$ and the present day (i.e. final time) temperature field $\mathbf{T}_{\text{obs}} = \mathbf{T}^{n_F}$. These data are then used in the optimization eq. (13) with the aim to recover the assumed initial temperature $\mathbf{T}_{\text{init}}$ and the true parameters $\mathbf{m}$ from these observations.

5 COMPUTATION OF ADJOINT-BASED DERIVATIVES

As discussed above, we follow a discretize-then-optimize approach to compute derivatives of $\hat{\mathcal{J}}(\mathbf{T}_{\text{init}}, \mathbf{m})$, defined in eq. (13), with respect to $(\mathbf{T}_{\text{init}}, \mathbf{m})$. For that purpose, we combine the discretized objective functional eq. (12), in which we consider all variables as independent, with

the discretized governing eq. (11), enforced through Lagrange multipliers. The resulting Lagrangian function is defined as

$$\begin{aligned}\mathcal{L}(\mathbf{T}_{\text{init}}, \mathbf{m}, \bar{\mathbf{T}}, \bar{\mathbf{u}}, \bar{\mathbf{p}}, \bar{\boldsymbol{\lambda}}, \bar{\mathbf{v}}, \bar{\mathbf{q}}) &= \mathcal{J}(\mathbf{T}_{\text{init}}, \mathbf{m}, \bar{\mathbf{T}}, \bar{\mathbf{u}}) + (\boldsymbol{\lambda}^0)^\mathsf{T}(\mathbf{T}_{\text{init}} - \mathbf{T}^0) \\ &+ \sum_{n=0}^{n_F} \begin{bmatrix} \mathbf{v}^n \\ \mathbf{q}^n \end{bmatrix}^\mathsf{T} \left(\begin{bmatrix} A^n & B \\ B^\mathsf{T} & 0 \end{bmatrix} \begin{bmatrix} \mathbf{u}^n \\ \mathbf{p}^n \end{bmatrix} - \begin{bmatrix} F\mathbf{T}^n \\ 0 \end{bmatrix} \right) \\ &+ \sum_{n=0}^{n_F-1} (\boldsymbol{\lambda}^{n+1/2})^\mathsf{T} \left[M_a^n \mathbf{T}^{n+1/2} - M_b^n \mathbf{T}^n \right] \\ &+ \sum_{n=0}^{n_F-1} \begin{bmatrix} \mathbf{v}^{n+1/2} \\ \mathbf{q}^{n+1/2} \end{bmatrix}^\mathsf{T} \left(\begin{bmatrix} A^{n+1/2} & B \\ B^\mathsf{T} & 0 \end{bmatrix} \begin{bmatrix} \mathbf{u}^{n+1/2} \\ \mathbf{p}^{n+1/2} \end{bmatrix} - \begin{bmatrix} F\mathbf{T}^{n+1/2} \\ 0 \end{bmatrix} \right) \\ &+ \sum_{n=0}^{n_F-1} (\boldsymbol{\lambda}^{n+1})^\mathsf{T} \left(M_c^n \mathbf{T}^{n+1} - M_d^n \mathbf{T}^n \right), \end{aligned} \tag{14}$$

where $\bar{\mathbf{v}} = (\mathbf{v}^0, \mathbf{v}^{1/2}, \mathbf{v}^1, \ldots, \mathbf{v}^{n_F})$, $\bar{\mathbf{q}} = (\mathbf{q}^0, \mathbf{q}^{1/2}, \ldots, \mathbf{q}^{n_F})$, $\bar{\boldsymbol{\lambda}} = (\boldsymbol{\lambda}^0, \boldsymbol{\lambda}^{1/2}, \ldots, \boldsymbol{\lambda}^{n_F})$ are the discrete adjoint velocity, pressure, and temperature, with superscripts indicating the time step. It follows from the theory of Lagrange multipliers (Gunzburger 2003; Nocedal & Wright 2006; Borzì & Schulz 2012) that, provided all derivatives of the Lagrangian function with respect to the dependent variables ($\bar{\mathbf{T}}$, $\bar{\mathbf{u}}$, $\bar{\mathbf{p}}$, $\bar{\boldsymbol{\lambda}}$, $\bar{\mathbf{v}}$, $\bar{\mathbf{q}}$) vanish, the derivatives of $\hat{\mathcal{J}}$ are the derivatives of the Lagrangian function with respect to the parameters ($\mathbf{T}_{\text{init}}$, $\mathbf{m}$). Setting each derivative of the Lagrangian with respect to ($\bar{\boldsymbol{\lambda}}$, $\bar{\mathbf{v}}$, $\bar{\mathbf{q}}$) to zero, reproduces the state eq. (11). Derivatives of the Lagrangian with respect to the state variables ($\bar{\mathbf{T}}$, $\bar{\mathbf{u}}$, $\bar{\mathbf{p}}$) are, for $n = 0, 1, \ldots, n_F$, given by:

$$\frac{\partial \mathcal{L}}{\partial \mathbf{u}^n} = \beta_S O^\mathsf{T} \left(O\mathbf{u}^n - \mathbf{u}^n_{\text{obs}} \right) + \left(\frac{\partial (A^n \mathbf{u}^n)}{\partial \mathbf{u}^n} \right)^\mathsf{T} \mathbf{v}^n + B\mathbf{q}^n - \left(\frac{\partial M_b^n}{\partial \mathbf{u}^n} \mathbf{T}^n \right)^\mathsf{T} \boldsymbol{\lambda}^{n+1/2} \chi_{n<n_F}, \tag{15a}$$

$$\frac{\partial \mathcal{L}}{\partial \mathbf{p}^n} = B^\mathsf{T} \mathbf{v}^n, \tag{15b}$$

$$\frac{\partial \mathcal{L}}{\partial \mathbf{T}^n} = \beta_F M(\mathbf{T}^{n_F} - \mathbf{T}_{\text{obs}}) \chi_{n=n_F} + \left(\frac{\partial A^n}{\partial \mathbf{T}^n} \mathbf{u}^n - F \right)^\mathsf{T} \mathbf{v}^n - \left(M_b^n \right)^\mathsf{T} \boldsymbol{\lambda}^{n+1/2} \chi_{n<n_F} \tag{15c}$$

$$- \left(M_d^n \right)^\mathsf{T} \boldsymbol{\lambda}^{n+1} \chi_{n<n_F} + \left(M_c^{n-1} \right)^\mathsf{T} \boldsymbol{\lambda}^n \chi_{n>0} + \beta_R K \left(\mathbf{T}^n - \mathbf{T}_{\text{mean}} \right) \chi_{n=0},$$

$$\frac{\partial \mathcal{L}}{\partial \mathbf{u}^{n+1/2}} = \left(\frac{\partial (A^{n+1/2} \mathbf{u}^{n+1/2})}{\partial \mathbf{u}^{n+1/2}} \right)^\mathsf{T} \mathbf{v}^{n+1/2} + B\mathbf{q}^{n+1/2} + \left(\frac{\partial M_c^n}{\partial \mathbf{u}^{n+1/2}} \mathbf{T}^{n+1} - \frac{\partial M_d}{\partial \mathbf{u}^{n+1/2}} \mathbf{T}^n \right)^\mathsf{T} \boldsymbol{\lambda}^{n+1}, \tag{15d}$$

$$\frac{\partial \mathcal{L}}{\partial \mathbf{p}^{n+1/2}} = B^\mathsf{T} \mathbf{v}^{n+1/2}, \tag{15e}$$

$$\frac{\partial \mathcal{L}}{\partial \mathbf{T}^{n+1/2}} = \left(M_a^n \right)^\mathsf{T} \boldsymbol{\lambda}^{n+1/2} + \left(\frac{\partial A^{n+1/2}}{\partial \mathbf{T}^{n+1/2}} \mathbf{u}^{n+1/2} - F \right)^\mathsf{T} \mathbf{v}^{n+1/2}, \tag{15f}$$

where $\chi_{c(n)} = 1$ if the condition $c(n)$ is satisfied, and $\chi_{c(n)} = 0$ if $c(n)$ is not satisfied. This indicator function χ allows a convenient notation. Setting all derivatives of the Lagrangian in eq. (15) to zero, we obtain the discrete adjoint equations, which are solved for the adjoint variables after the state variables ($\bar{\mathbf{T}}$, $\bar{\mathbf{u}}$, $\bar{\mathbf{p}}$) have been computed. These discrete adjoint equations are, for $n = 0, \ldots, n_F$ as follows:

$$\begin{bmatrix} \frac{\partial (A^n \mathbf{u}^n)}{\partial \mathbf{u}^n} & B \\ B^\mathsf{T} & 0 \end{bmatrix}^\mathsf{T} \begin{bmatrix} \mathbf{v}^n \\ \mathbf{q}^n \end{bmatrix} = \begin{bmatrix} -\beta_S O^\mathsf{T} \left(O\mathbf{u}^n - \mathbf{u}^n_{\text{obs}} \right) + \left(\frac{\partial M_b^n}{\partial \mathbf{u}^n} \mathbf{T}^n \right)^\mathsf{T} \boldsymbol{\lambda}^{n+1/2} \chi_{n<n_F} \\ \mathbf{0} \end{bmatrix}, \tag{16a}$$

$$\left(M_c^{n-1} \right)^\mathsf{T} \boldsymbol{\lambda}^n \chi_{n>0} = -\beta_F M(\mathbf{T}^{n_F} - \mathbf{T}_{\text{obs}}) \chi_{n=n_F} - \left(\frac{\partial A^n}{\partial \mathbf{T}^n} \mathbf{u}^n - F \right)^\mathsf{T} \mathbf{v}^n + \left(M_b^n \right)^\mathsf{T} \boldsymbol{\lambda}^{n+1/2} \chi_{n<n_F} + \left(M_d^n \right)^\mathsf{T} \boldsymbol{\lambda}^{n+1} \chi_{n<n_F} \tag{16b}$$

$$-\beta_R K \left(\mathbf{T}^n - \mathbf{T}_{\text{mean}} \right) \chi_{n=0},$$

$$\begin{bmatrix} \frac{\partial A^{n+1/2} \mathbf{u}^{n+1/2}}{\partial \mathbf{u}^{n+1/2}} & B \\ B^\mathsf{T} & 0 \end{bmatrix}^\mathsf{T} \begin{bmatrix} \mathbf{v}^{n+1/2} \\ \mathbf{q}^{n+1/2} \end{bmatrix} = \begin{bmatrix} -\left(\frac{\partial M_c^n}{\partial \mathbf{u}^{n+1/2}} \mathbf{T}^{n+1} - \frac{\partial M_d^n}{\partial \mathbf{u}^{n+1/2}} \mathbf{T}^n \right)^\mathsf{T} \boldsymbol{\lambda}^{n+1} \\ \mathbf{0} \end{bmatrix}, \tag{16c}$$

$$\left(M_a^n \right)^\mathsf{T} \boldsymbol{\lambda}^{n+1/2} = -\left(\frac{\partial A^{n+1/2}}{\partial \mathbf{T}^{n+1/2}} \mathbf{u}^{n+1/2} - F \right)^\mathsf{T} \mathbf{v}^{n+1/2}. \tag{16d}$$

For the adjoint temperature $\bar{\boldsymbol{\lambda}}$, no initial, but a final time condition is available from eq. (16b) with $n = n_F$. Thus, the adjoint mantle flow equations must be solved backwards in time, which is typical for adjoints for time-dependent problems. Thus, we compute ($\mathbf{v}^{n_F}$, $\mathbf{q}^{n_F} \boldsymbol{\lambda}^{n_F}$), then

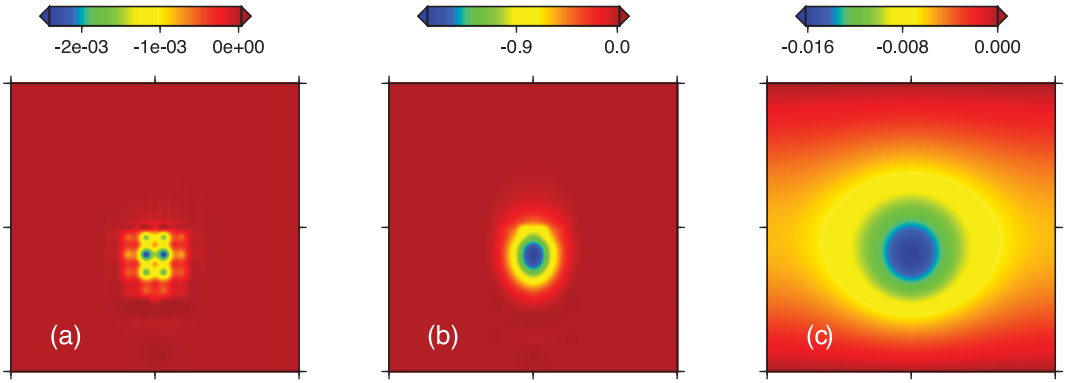

Figure 1. Gradients with respect to different inner products for the temperature initial condition inversion presented in Section 8. (a) Euclidean gradient $\mathbf{g}$, (b) gradient $\mathbf{g}_M$ obtained with mass matrix-weighted inner product and (c) gradient $\mathbf{g}_K$ obtained with stiffness matrix-weighted inner product.

$(\mathbf{v}^{n_F-1/2}, \mathbf{q}^{n_F-1/2}\boldsymbol{\lambda}^{n_F-1/2})$, and so on. Finally, we obtain $(\mathbf{v}^0, \mathbf{q}^0, \boldsymbol{\lambda}^0)$. In these equations, the coupling between forward and adjoint variables is a crucial part of the adjoint theory, as also noted by Horbach *et al.* (2014). Comparing the adjoint system eq. (16) with the forward system eq. (11), we observe that the adjoint equations use the same convection velocity as the forward solution. Moreover, the same effective viscosity is used in the construction of the stress blocks A in the adjoint system, which thus does not depend on adjoint variables. Hence, the adjoint equations are linear in the adjoint variables $(\bar{\boldsymbol{\lambda}}, \bar{\mathbf{v}}, \bar{\mathbf{q}})$. Finally the derivatives with respect to the parameters $\mathbf{T}_{\text{init}}$ and $\mathbf{m}$ are obtained by taking derivatives of the Lagrangian function, which results in

$$\frac{\partial \hat{\mathcal{J}}}{\partial \mathbf{T}_{\text{init}}} = \frac{\partial \mathcal{L}}{\partial \mathbf{T}_{\text{init}}} = \boldsymbol{\lambda}^0, \tag{17a}$$

$$\frac{\partial \hat{\mathcal{J}}}{\partial \mathbf{m}} = \frac{\partial \mathcal{L}}{\partial \mathbf{m}} = \sum_{n=0}^{n_F} \left[\frac{\partial}{\partial \mathbf{m}} A^n \mathbf{u}^n\right]^\intercal \mathbf{v}^n + \left[\frac{\partial}{\partial \mathbf{m}} A^{n+1/2} \mathbf{u}^{n+1/2}\right]^\intercal \mathbf{v}^{n+1/2} \chi_{n<n_F}. \tag{17b}$$

In the above equations, most matrices do not need to be assembled explicitly, but only their products with vectors are required. Detailed expressions for the partial derivatives are shown in the Appendix. In the next section, we discuss interpretation of these derivatives and different ways they can be represented by vectors.

6 DERIVATIVES, GRADIENTS AND FINITE-DIFFERENCE VERIFICATION

In this section, we recall definitions and discuss the difference between derivatives and gradients. While this difference is sometimes overlooked, the related scaling and pre-conditioning of gradients plays an important role for the convergence of gradient-based optimization algorithms if the optimization variables originate from the discretization of a continuous field. Assume that the objective functional $\hat{\mathcal{J}} : X \to \mathbb{R}$ is differentiable, and $X = X_T \times X_m$, with X_T is the space for the (discretized) initial temperature $\mathbf{T}_{\text{init}}$, and X_m is the space for the parameter vector $\mathbf{m}$. The derivative $\mathcal{J}'(\mathbf{T}_{\text{init}}, \mathbf{m}) = [\partial\hat{\mathcal{J}}/\partial\mathbf{T}_{\text{init}}, \partial\hat{\mathcal{J}}/\partial\mathbf{m}]$ is a linear functional acting on elements in X, that is, the directional derivative $\hat{\mathcal{J}}'(\mathbf{T}_{\text{init}}, \mathbf{m})(\tilde{\mathbf{T}}_{\text{init}}, \tilde{\mathbf{m}}) \in \mathbb{R}$ is uniquely defined for all $(\tilde{\mathbf{T}}_{\text{init}}, \tilde{\mathbf{m}}) \in X$. In a gradient-based descent algorithm for $\hat{\mathcal{J}}$, we require a vector representation of this derivative. For that purpose, one uses an inner product $(\,\cdot\,, \cdot)_X$ on X, and computes the gradient vector $\mathbf{g}$ as the representative of the derivative with respect to that inner product, that is, $\mathbf{g}$ must satisfy $\mathcal{J}'(\mathbf{T}_{\text{init}}, \mathbf{m})(\tilde{\mathbf{T}}_{\text{init}}, \tilde{\mathbf{m}}) = (\mathbf{g}, (\tilde{\mathbf{T}}_{\text{init}}, \tilde{\mathbf{m}}))_X$ for all directions $(\tilde{\mathbf{T}}_{\text{init}}, \tilde{\mathbf{m}})$. In particular, $\mathbf{g}$ depends on the choice of inner product (see also, e.g. Borzì & Schulz 2012). Thus, this choice influences the convergence behaviour of a gradient-based descent algorithm.

To illustrate the dependence of the gradient on the inner product, we now assume that the objective functional $\hat{\mathcal{J}}$ only depends on the discretized initial temperature $\mathbf{T}_{\text{init}}$, whose components are coefficients for a finite element basis. A natural choice for an inner product between finite-dimensional variables is the Euclidean inner product, that is, $\mathcal{J}'(\mathbf{T}_{\text{init}})(\tilde{\mathbf{T}}_{\text{init}}) = (\mathbf{g}, \tilde{\mathbf{T}}_{\text{init}}) = \mathbf{g}^\intercal \tilde{\mathbf{T}}_{\text{init}}$. Note that the components of the resulting Euclidean gradient $\mathbf{g}$ depend on the (local) refinement of the mesh. In particular, the individual components must tend to zero as the mesh is refined. Thus, the Euclidean gradient $\mathbf{g}$ does not represent a finite element discretization of a continuous gradient 'function', and the relative magnitude of its components depends on the local mesh refinement. This can be problematic for a gradient-based descent algorithm, in particular for locally refined meshes. Consider now an inner product that is weighted by a symmetric, positive-definite matrix W, that is, $(x, y)_W := x^\intercal W y$. The corresponding gradient $\mathbf{g}_W$ satisfies $\mathcal{J}'(\mathbf{T}_{\text{init}})(\tilde{\mathbf{T}}_{\text{init}}) = \mathbf{g}_W^\intercal W \tilde{\mathbf{T}}_{\text{init}}$ and thus $\mathbf{g}_W = W^{-1}\mathbf{g}$. In particular, the Euclidean product corresponds to the identity weighting matrix $W = I$, and thus $\mathbf{g} = \mathbf{g}_I$. For $W := M$, the mass matrix, the corresponding inner product approximates an L^2-inner product and thus the gradient $\mathbf{g}_M$ contains finite element coefficients of a gradient function (provided the infinite-dimensional gradient is smooth). The choice $W = K$, the stiffness matrix, results in $\mathbf{g}_K = K^{-1}\mathbf{g}$, which is smoother than $\mathbf{g}_M$. This choice ensures a smooth gradient, which can be useful in applications. For illustration, Fig. 1 shows a comparison of these different representations of the derivative for the initial condition inversion discussed in detail in Section 8. If we were able to choose $W = H(\mathbf{T}_{\text{init}}^k)$, the Hessian at some

Table 1. Comparison between adjoint-based and finite-difference derivatives for sinking cylinder problem from Section 8.

ϵ	$\frac{\partial \hat{\mathcal{J}}}{\partial \mathbf{T}_{\text{init}}}(\tilde{T}^{\text{r}}_{\text{init}})$	$\frac{\partial \hat{\mathcal{J}}}{\partial C}$	$\frac{\partial \hat{\mathcal{J}}}{\partial n}$	$\frac{\partial \hat{\mathcal{J}}}{\partial E}$
1e-02	3.5220e-02	-9.2172e-03	1.9622e-02	4.2110e-03
1e-03	4.0388e-02	-8.9323e-03	2.1406e-02	4.2795e-03
1e-04	4.0888e-02	-8.9032e-03	2.1580e-02	4.2863e-03
Adjoint-based	4.0944e-02	-8.9000e-03	2.1600e-02	4.2871e-03

initial temperature estimate $\mathbf{T}^k_{\text{init}}$ (which we assume to be positive definite), then the resulting gradient is $\mathbf{g}_H = H(\mathbf{T}_{\text{init}})^{-1}\mathbf{g}$, which is the Newton direction. While this choice requires second derivatives, it corresponds to fast local convergence. All gradient representations with positive definite weight matrices W are descent direction and can thus be used in gradient-based optimization algorithms, but the performance of this algorithm depends heavily on the choice of the inner product. Ideally, the weighting matrix in the inner product for the initial temperature should be the Hessian matrix or an approximation thereof. In the descent algorithm discussed in the next section, we compare different gradient representations and their behaviour. There, the inner product weight matrix W appears as initialization matrix R_0 in the quasi-Newton algorithm, which aims at iteratively approximating second derivative information.

Finally, we numerically verify the gradient expressions derived in the previous section using finite differences. This is critical to ensure correctness of derivation and implementation of the adjoint equations and the gradient expressions. We have derived our gradients as accurately as possible by limiting the number of approximations. However, there are two instances where approximations were unavoidable. First, because of the min -function in the viscosity law eq. (3), the derivative is not unique at points where the expression under the min -function is zero. At these points, we decide to set the gradient to zero. Secondly, in eq. (6), the parameter τ in the SUPG scheme is a function of $\boldsymbol{u}$ and we neglect this dependence in the adjoint equations. However, since τ is small, discarding $\partial\tau/\partial\boldsymbol{u}$ terms has a negligible effect. In addition, the numerical solution of the linear and nonlinear systems uses iterative methods which can introduce errors. Despite these minor approximations, we can demonstrate the correctness and accuracy of the derivatives obtained from the adjoint model. The finite difference test is the most straightforward means to accomplish this.

For that purpose, we choose a random direction $\tilde{\mathbf{T}}^{\text{r}}_{\text{init}}$, and compare the directional derivatives

$$\frac{\hat{\mathcal{J}}(\mathbf{T}_{\text{init}} + \epsilon\tilde{\mathbf{T}}^{\text{r}}_{\text{init}}, \mathbf{m}) - \hat{\mathcal{J}}(\mathbf{T}_{\text{init}}, \mathbf{m})}{\epsilon} \sim \frac{\partial \hat{\mathcal{J}}}{\partial \mathbf{T}_{\text{init}}}\left(\tilde{\mathbf{T}}^{\text{r}}_{\text{init}}\right) = \mathbf{g}_W^{\mathsf{T}} W \tilde{\mathbf{T}}^{\text{r}}_{\text{init}},$$

$$\frac{\hat{\mathcal{J}}(\mathbf{T}_{\text{init}}, \mathbf{m} + \epsilon\mathbf{e}_i) - \hat{\mathcal{J}}(\mathbf{T}_{\text{init}}, \mathbf{m})}{\epsilon} \sim \frac{\partial \hat{\mathcal{J}}}{\partial \mathbf{m}_i},$$

where $\mathbf{m}_i$ is the ith rheology parameter, $\mathbf{e}_i$ denotes the ith unit vector, and W is a symmetric and positive definite weight matrix. As we reduce ϵ, the difference between the left and the right sides in the equation above should become progressively smaller. Note that the inner product used on the right-hand side of these gradient expressions must be consistent with the product used to derive the gradient vector from the derivative. Table 1 shows comparisons for derivatives with respect to the initial temperature and with respect to viscosity parameters for $W = I$. Indeed, reducing ϵ, the finite difference directional derivatives approach the directional derivatives computed using the adjoint equations. Note that when ϵ is decreased significantly below 10^{-4}, finite-difference gradients cannot be expected to be accurate as round-off errors start to dominate the result.

7 PRE-CONDITIONED LBFGS OPTIMIZATION

In addition to gradients, efficient solution methods for large-scale minimization problems such as eq. (13) ideally also incorporate second-order derivatives (i.e. Hessians) of the objective functional $\hat{\mathcal{J}}$ with respect to the parameters. While second-order directional derivatives can be obtained through the solution of appropriately modified state and adjoint equations (sometimes called incremental equations) (Borzì & Schulz 2012; Ratnaswamy *et al.* 2015), second-order derivative information can also be approximated using gradients computed during the optimization algorithm. The BFGS update formula and its limited-memory variant LBFGS are prominent examples of this approach (Nocedal & Wright 2006). We use the LBFGS method, which starts from a positive definite and symmetric initial inverse Hessian estimate R_0, and computes rank-2 updates for the inverse Hessian approximation in every iteration. The resulting approximation at the kth step, R_k, can then be used to compute an approximate Newton direction and update the parameters as follows:

$$\left[\mathbf{T}^{k+1}_{\text{init}}, \mathbf{m}^{k+1}\right] = \left[\mathbf{T}^{k}_{\text{init}}, \mathbf{m}^{k}\right] - \lambda R_k \mathbf{g}^k,$$

where $\mathbf{T}^k_{\text{init}}$ and $\mathbf{m}^k$ are the estimates for the initial temperature and the rheology parameters in the kth optimization iteration. Moreover, $\mathbf{g}^k$ is the (Euclidean) gradient of $\hat{\mathcal{J}}$ at $(\mathbf{T}^k_{\text{init}}, \mathbf{m}^k)$, and $\lambda > 0$ is the step size derived from a line search. To calculate the quasi-Newton direction $R_k\mathbf{g}^k$, a two-loop recursion can be used (see algorithm 7.4 of Nocedal & Wright 2006), which only requires the application of R_0 to vectors and does not require storage of the inverse Hessian approximation (which is usually a dense matrix), but only stores a fixed number of gradients that arise during the optimization. In finite-dimensional optimization, one commonly uses a scaled identity matrix γI for R_0, with γ being an appropriately computed scalar. If a better approximation of the inverse Hessian (or a part of the inverse Hessian) is available, it should be

used for R_0. While we do not compute the Hessian of the misfit part of the cost functional in our problem, we explicitly know the Hessian of the regularization term for the initial temperature, namely the (scaled) stiffness matrix K. While K is usually a better approximation to the true Hessian than the scaled identity matrix, incorporating K^{-1} in R_0 also smooths the search direction, and thus avoids mesh artefacts in the update direction. This often accelerates the convergence of the minimization algorithm, as illustrated later. To summarize, we use the inverse Hessian initialization

$$R_0 = \begin{bmatrix} \gamma_2 K^{-1} & 0 \\ 0 & \gamma_1 I \end{bmatrix},$$

where $\gamma_1 I$ corresponds to the rheology parameter vector m, and $\gamma_2 K^{-1}$ to initial temperature vector. In our implementation, we choose the scaling values $\gamma_1 = \gamma$, and γ_2 such that $\|R_0 \mathbf{g}^k\|_2 = \|\gamma_2 \mathbf{g}^k\|_2$.

8 SINKING CYLINDER PROBLEM

Our first example is that of a sinking cold cylinder (a circle in two dimensions) embedded in a homogeneous temperature background. Although simplified from a more realistic, spatially and rheologically complex subduction dynamics problem, the sinking cylinder problem has many of the same characteristics. The cold blob in the initial temperature field is given by a 2-D Gaussian, that is, the temperature-induced variations in viscosity are smooth. The domain is a unit box. We assume that the viscosity is temperature-dependent and strain-rate-dependent, with non-dimensional activation energy $E = 9$ and strain rate exponent $n = 2$. We use a constant pre-factor of $C = 1000$, $\sigma_{\text{yield}} = \infty$, $\eta_{\text{min}} = 10^{-2}$, $\eta_{\text{max}} = 10^3$ in eq. (3), and the Rayleigh number $\text{Ra} = 10^6$. We use a locally refined mesh that resolves the gradients of the temperature at the initial time and during the forward computation, which results in a mesh has 1165 degrees of freedom for temperature, 2330 for velocity, and 301 for pressure. The mesh is kept fixed in time for the forward computation, and also during the inversion process. As can be seen in Fig. 2, the cylinder descends through the fluid layer, and the surface velocity decreases over time.

Using synthetic observational data from a forward simulation with assumed initial temperature and rheological parameters, we first conduct an inversion to recover the initial temperature, assuming the viscosity parameters to be known. Note that the effective viscosity depends on the temperature and the strain rate and thus on the initial temperature. As an initial guess for the inversion, we use the uniform temperature $T_{\text{guess}} \equiv 1$ and we assume that the final time is reached after 50 time steps. Components occurring in the adjoint-based inversion are shown in Fig. 3, where (a) to (e) are forward state and adjoint temperature fields and the gradients for the first iteration, while (f) to (j) correspond to the converged last iteration. Starting from the homogeneous guess T_{guess} (a) for the initial condition, the final temperature T^{50} (b) is unchanged from $\mathbf{T}_{\text{init}}$ since for constant temperature there are no buoyancy forces. The adjoint temperature at the final time, $\boldsymbol{\lambda}^{50}$ (c), is indicative of the misfit between T^{50} and T^{50}_{data}. The adjoint temperature at the initial time, $\boldsymbol{\lambda}^1$ (d), is the back-propagated misfit to the first time step by solving the adjoint equations. Because the adjoint temperature convects using the forward modelling velocity, which is zero in this case, $\boldsymbol{\lambda}^1$ coincides with $\boldsymbol{\lambda}^{50}$. Then, the Euclidean gradient $\mathbf{g}$ (e) is calculated, and used to update our initial temperature guess. After 500 function evaluations, where each function evaluation consists of a full forward and a full adjoint calculation, the inversion converges to an initial temperature $\mathbf{T}_{\text{init}}$ (f). The corresponding final temperature T^{50} and surface velocities (g) are close to the true model, and $\boldsymbol{\lambda}^1$ (h) convects from $\boldsymbol{\lambda}^{50}$ (i) using almost the correct backward velocity. The magnitude of the Euclidean gradient (j) is also reduced greatly compared to the first iteration (e).

The gradients shown in Figs 3(e) and (j) are computed to represent the derivatives with respect to the Euclidean inner product—see the discussion in Section 6. Thus, they have a distinctly mottled appearance that reflects the underlying mesh structure. When using an identity matrix for the inverse Hessian approximation R_0 in the LBFGS method, the initial temperature $\mathbf{T}_{\text{init}}$ is updated using this Euclidean gradient $\mathbf{g}$, and thus these mesh-related artefacts also appear in the iterates for the initial conditions in Fig. 4 — however, they vanish at convergence.

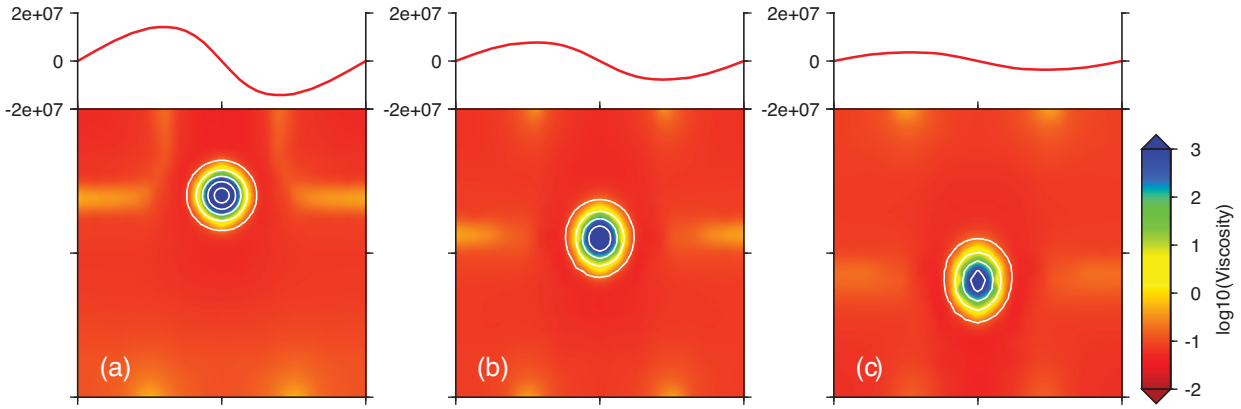

Figure 2. Forward simulation of the sinking cylinder model. The images show, from (a) to (c), the effective viscosity (in log10 scale) after 0, 25 and 50 time steps. Temperature contours for $T = 0.1$, 0.3, 0.5, 0.7 and 0.9 are shown with white lines. The non-dimensional surface horizontal velocity is shown as the red curve above the viscosity images.

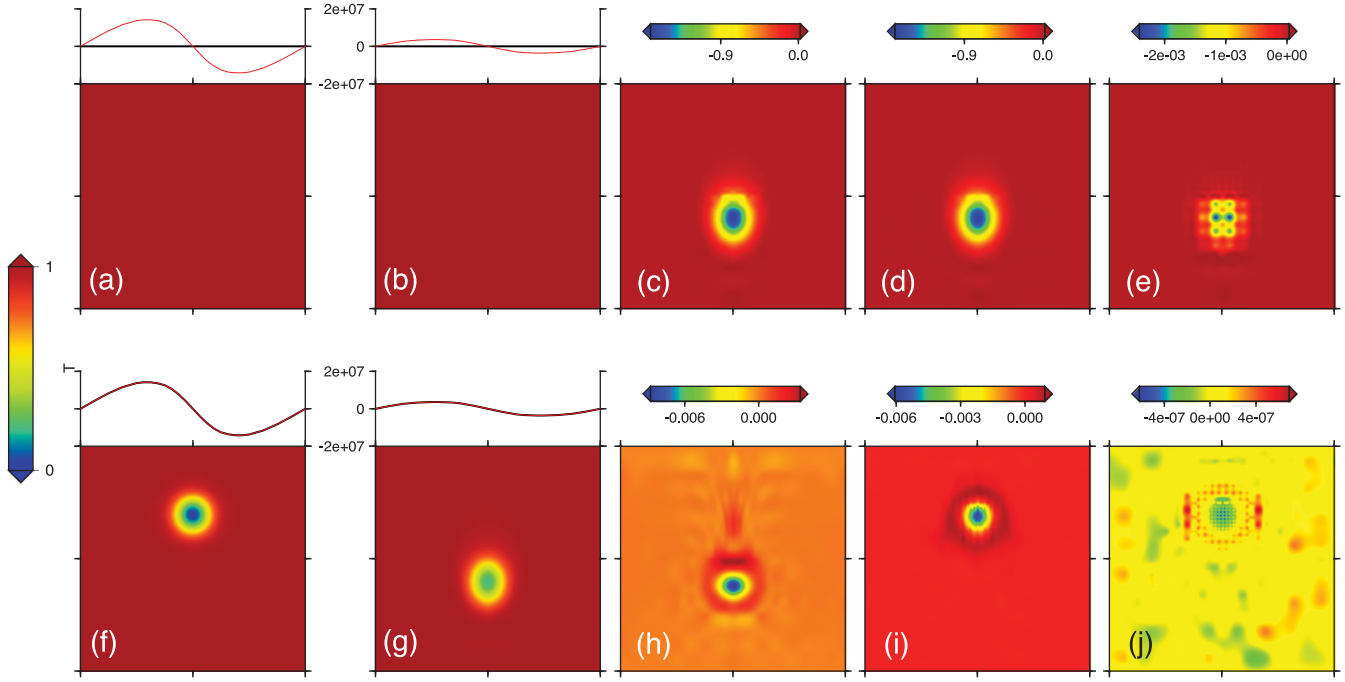

Figure 3. Inversion of the initial temperature for the falling cylinder problem. (a) to (e) show components occurring in the adjoint-based inversion method at the first function evaluation, that is, for the initial guess, where (a) corresponds to the initial temperature $\mathbf{T}_{\text{init}}$, (b) to the temperature T^{50} at the final time, (c) the final adjoint temperature $\boldsymbol{\lambda}^{50}$, (d) the initial adjoint temperature $\boldsymbol{\lambda}^{1}$, and (e) the Euclidean gradient $\mathbf{g}$ with respect to the initial condition. (f) to (g) show the analogous fields for the 500th function evaluation, that is, the converged solution. The curves above the first two columns show the surface velocity at initial and final times. The red curve shows the data, and the black curve the velocity computed with the temperature at those instances.

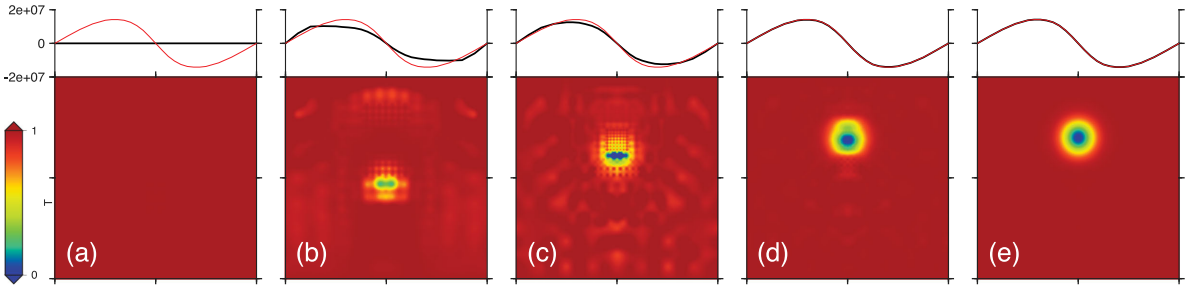

Figure 4. Convergence history for $\mathbf{T}_{\text{init}}$-only inversion using the Euclidean gradient $\mathbf{g}$, that is, a scaled identity matrix as inverse Hessian approximation R_0 in the LBFGS methods (see Section 7). The images (a)–(e) show the iterates for the initial temperature $\mathbf{T}^k_{\text{init}}$ after $k = 2$, 20, 70, 200 and 500 function evaluations.

Instead of using an identity matrix, an inverse mass or stiffness matrix for R_0 corresponds to the representation of derivatives in a different inner product and thus avoids mesh artefacts as in Fig. 5 (see also Fig. 1). While all of these LBFGS variants eventually converge to the same solution as demonstrated by the several orders of magnitude reduction in misfit and gradient norms (see Fig. 6), the choice of R_0 and correspondingly, the inner product in which to represent the derivative, influences the speed of convergence. In particular, we find that using the (scaled) inverse stiffness matrix for the initial inverse Hessian approximation R_0 leads to faster convergence.

Next, we assume that the initial temperature is known and we invert for the rheology parameters only. Instead of fitting a single velocity profile for a single time, that is, the instantaneous inversion as in Worthen *et al.* (2014) and Ratnaswamy *et al.* (2015), we incorporate the entire surface velocity data history and the final temperature. For the recovery of the viscosity parameters, we conduct an inversion for the pre-factor C and nonlinear exponent n. The recovery is nearly perfect in this case, and the iterates for C and n converge to the true values in less than 40 function evaluations (Fig. 7).

Having demonstrated recovery of the initial temperature knowing the constitutive parameters and recovery of the constitutive parameters knowing the initial temperature, we now attempt a joint inversion of the initial temperature and the two viscosity parameters, C and n (having true values of 1000 and 2, respectively). In the first case, starting from a constant temperature guess ($T_{\text{guess}} \equiv 1$) and constitutive parameters $C_{\text{guess}} = 300$ and $n_{\text{guess}} = 2.5$, the inversion stops after 220 function evaluation, with $C = 993.0$ and $n = 1.996$, close to the actual values. In the second case, starting from $T_{\text{guess}} \equiv 1$ and $C_{\text{guess}} = 500$ and $n_{\text{guess}} = 2.5$, the inversion stops after 280 function evaluation with $C = 1416.3$ and $n = 2.135$, distinctly different from the true values. The convergence history for C and n differs for the two joint inversion cases (Fig. 8). Although the two cases yield comparable reductions of the objective functional, they lead to two different recovered values of C and n. This

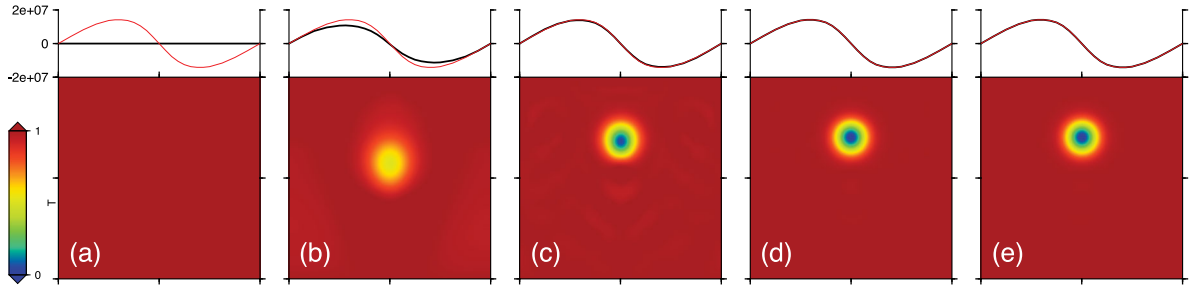

Figure 5. Convergence history for the $\mathbf{T}_{\text{init}}$-only inversion using the gradient $\mathbf{g}_K$, that is, a scaled stiffness matrix as inverse Hessian approximation R_0 in the LBFGS methods (see Section 7). The images (a) to (e) show the iterates for the initial temperature $\mathbf{T}^k_{\text{init}}$ for $k = 2$, 20, 70, 200 and 500 function evaluations.

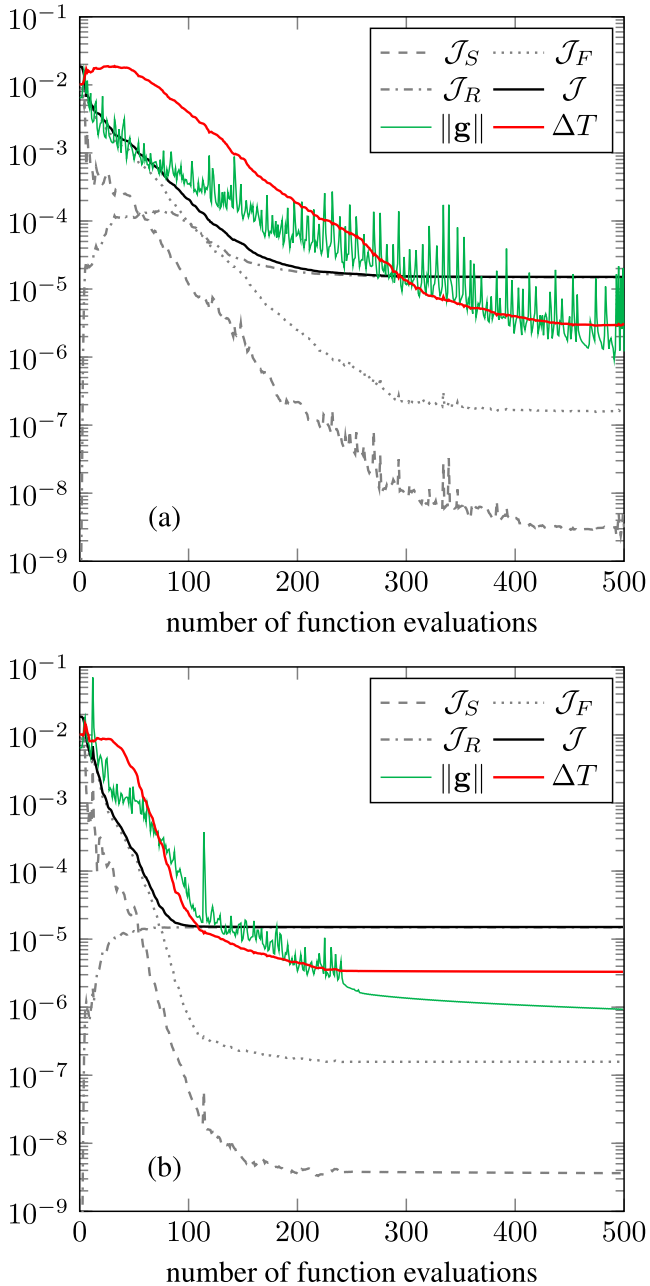

Figure 6. Reduction of objective and gradient norm for cylinder sinker problem using LBFGS with (a) a scaled identity matrix pre-conditioner, and with (b) a pre-conditioner R_0 given by the stiffness matrix. The curves correspond to surface misfit $\mathcal{J}_S$, final temperature misfit $\mathcal{J}_F$, regularization term $\mathcal{J}_R$, total cost $\mathcal{J} = \mathcal{J}_S + \mathcal{J}_F + \mathcal{J}_R$ and norm of the Euclidean gradient $\|\mathbf{g}\|$, and a measure for the difference between iterates and true initial temperature $\Delta T = (\mathbf{T}^k_{\text{init}} - \mathbf{T}_{\text{true}})^\intercal M(\mathbf{T}^k_{\text{init}} - \mathbf{T}_{\text{true}})$.

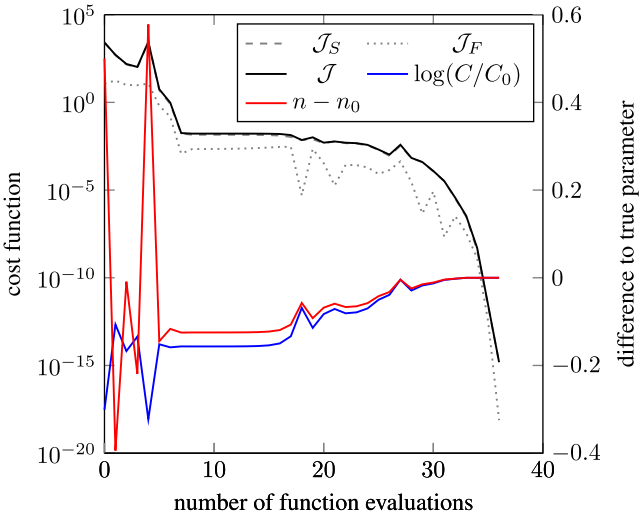

Figure 7. Reduction of objective and convergence of C and n for cylinder sinker problem. $\mathcal{J}_S$, $\mathcal{J}_F$ and $\mathcal{J}$ are shown on left axis, while $\log(C/C_0)$ and $n - n_0$ are shown on right axis, with C_0, n_0 being the true values of pre-factor and nonlinear exponent.

shows that the problem is ill-posed and is a consequence of not using regularization [or the incorporation of prior information in the context of Bayesian inversion as in Ratnaswamy *et al.* (2015)] for the rheology parameters. This ill-posedness leads to a strong trade-off between the quantities we wish to find geophysically, since for this simple model configuration different C and n given rise to nearly identical effective viscosities. To show that the different recovered C and n fit the data equally well, we observe that the recovered temperature, surface velocity, and corresponding effective viscosity for the two cases are nearly identical (Fig. 9). We also compare the total viscous dissipation at the initial temperature, defined as $\int 2\eta_{\text{eff}}(\boldsymbol{u}, T)D(\boldsymbol{u}) : D(\boldsymbol{u})\mathrm{d}\Omega$, for these two cases. The first case has a dissipation of 1.883×10^8, the second case 1.886×10^8, and the true model 1.889×10^8, that is, they are essentially identical.

We have attempted to isolate the differences occurring in the previous two cases by exploring the influence of the rheology parameters C and n in the inversion. Assuming the initial temperature is known, we vary C and n, calculate the forward solution and evaluate the cost function. To simplify the problem even further, we plot contours of $\mathcal{J}_S$ that arise from an instantaneous ($n_F = 0$) model (Fig. 10). We observe a narrow flat valley in this objective along a specific direction in the C–n plane, indicative of a strong trade-off in this direction. Similar results hold for $\mathcal{J}_F$, and for time-dependent models (e.g. $n_F = 50$).

Plotting the rheology parameter iterates for the (C, n)-only inversion (Fig. 7) and the two ($\mathbf{T}_{\text{init}}$, C, n) joint inversions (Fig. 8) along with the cost function contours, we find that the optimization algorithm spends many iterations navigating within this 'trade-off valley' (Fig. 10). With initial temperature known, the iterates quickly lie in the narrow valley and then converge to the true minimum. If the initial temperature also has to be recovered, the parameter space is significantly larger. With every change of the initial temperature iterate T^k_{init}, the trade-off valley is perturbed, which makes it more challenging to converge to the true minimum.

In this cylinder model, the strong trade-off is partially due to the simplicity of this problem, where the pre-factor C and nonlinear exponent n influence the effective viscosity similarly. In a more complex model, the difference between the influence of C and n on the effective viscosity is stronger, and the trade-offs are likely reduced.

9 SUBDUCTION PROBLEM

Plate motions are intimately tied to subduction, and changes in plate motion are thought to be, at least partially, controlled by changes in subduction (including initiation, slab dip, the age of the subducting plate, the depth of slab penetration, and subduction termination) (Zhong & Gurnis 1995b; Billen 2008; Stadler *et al.* 2010; Gerya 2011). Consequently, we have designed a model in which changes in plate motion and subduction are important aspects of the dynamics, while being sufficiently compact that we can explore the forward and inverse problems with moderate computing resources. We focus on an important component of the time-dependence of plate motions, namely the progressive migration of a mid-ocean ridge toward an oceanic trench, as occurred off the west coast of North America with the eastward motion of the Farallon-Pacific ridge towards the subduction zone at the continental margin during the Cenozoic (Atwater 1970). Burkett & Billen (2009) formulated fully dynamic, forward convection models meant to study this process, specifically tailored to the Miocene evolution of Baja California in which the Farallon-Pacific ridge stalled before reaching the trench.

Within a domain of 2000 km × 1000 km, we set a mid-ocean ridge 500 km to the left of a subducting slab with an initial dip of about 45° (see Fig. 11a). The temperature boundary condition at the top of the domain is $T_d = 0$, while it is $T_d = 1$ at its bottom. The thermal structure of the lithosphere is derived from a half-space cooling model, assuming that the plate age increases linearly from 0 Myr at the ridge to 30 Myr at the trench and from the ridge to the left edge of the domain. The upper plate is assumed to be initially 30 Myr. The initial slab was created by assuming its temperature gradually warms with depth, in which a weak zone curves around along the top of the thermal slab similar to the problem setup in Ratnaswamy *et al.* (2015). The viscosity in the upper mantle is non-Newtonian, with $n_1 = 3$, while in the lower

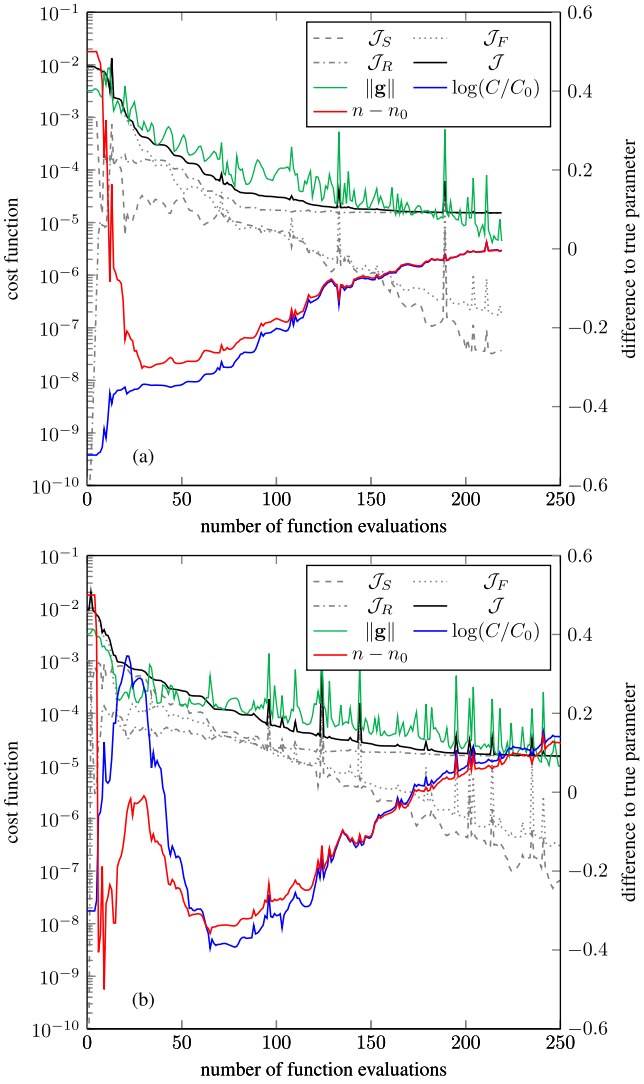

Figure 8. Convergence of inversion for initial temperature and viscosity parameters in cylinder sinker problem. Shown are the reduction of terms in the objective and the gradient norm, and iterates for the rheology parameters C, n for inversion case 1 (a) and case 2 (b). Legend meaning is the same as in Figs 6 and 7. Note that the reduction in the objective is of similar order, while the recovered C and n differ.

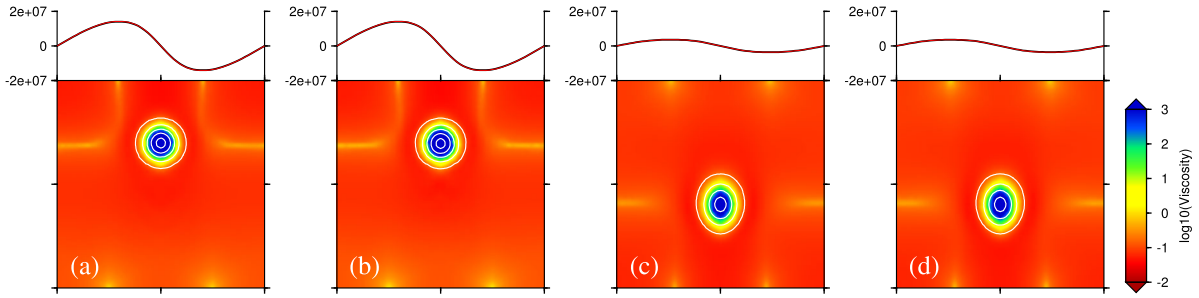

Figure 9. Recovered effective viscosity, temperature contour and surface velocity for two joint inversion cases with different initializations. (a) and (c) correspond to 0 and 50 time step of the last function evaluation in case 1. (b) and (d) correspond to 0 and 50 time step of the last function evaluation in case 2.

mantle it is Newtonian, that is, $n_2 = 1$. The temperature-dependence of viscosity is controlled by a non-dimensional activation energy with $E = 9$ through the whole domain. The pre-factor is $C_1 = 3 \times 10^4$ in the upper mantle (depths <410 km), $C_2 = 6 \times 10^4$ in the transition zone (410–660 km), and $C_3 = 2 \times 10^3$ in lower mantle (>660 km). We set $\sigma_{\text{yield}} = 300$ MPa, $\eta_{\text{min}} = 10^{18}$ Pa s, $\eta_{\text{max}} = 10^{23}$ Pa s. In the forward computation and inversion, we use a fixed non-uniform mesh, where the top 100 km boundary layer and the slab subduction region are refined (down to a mesh size of about 8 km), with 43 445 degrees of freedom for temperature, 86 890 for velocity and 10 963 for pressure.

As expected from similar published models (Burkett & Billen 2009), the centre oceanic plate moves to the right with a velocity of 55–60 mm yr^{-1}, initially (see Fig. 11a). The large induced shear in the upper mantle below the oceanic lithosphere and around the slab lowers

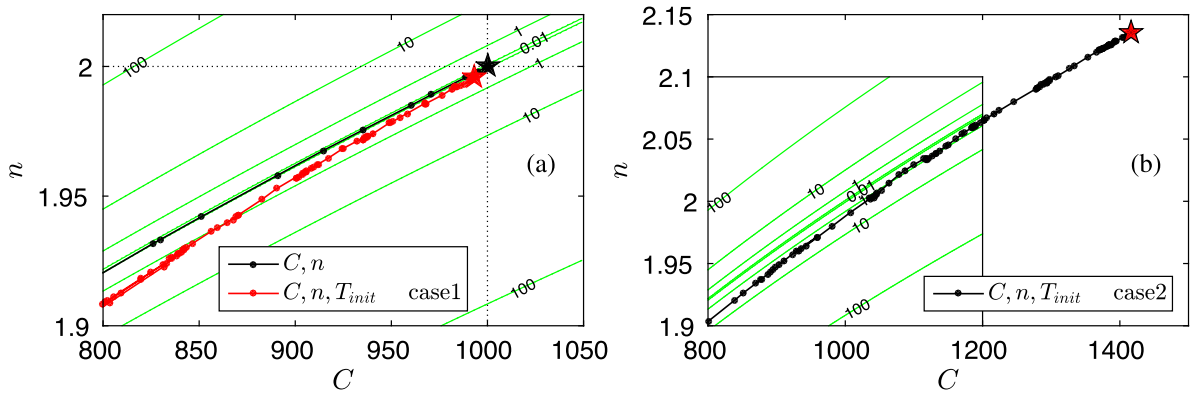

Figure 10. $\mathcal{J}_S$ contours and C, n inversion iterates. Green lines show $\mathcal{J}_S$ contours of 0.01, 1, 10, and 100 for a $n_F = 0$, true T_{true} known case. (a) Rheology parameter iterates for (C, n)-only inversion (see Fig. 7), and for (C, n, $\mathbf{T}_{\text{init}}$)-joint inversion case 1 (Fig. 8); (b) Rheology parameter iterates for (C, n, $\mathbf{T}_{\text{init}}$) joint inversion case 2 (8).

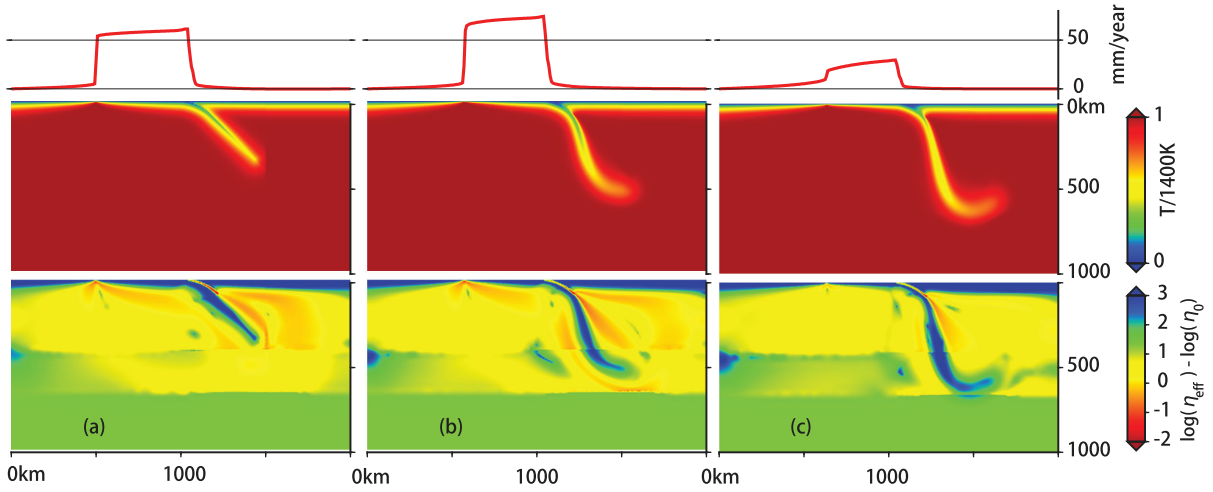

Figure 11. Subduction forward modelling at (a) 0, (b) 25, and (c) 50th time step, corresponding to 0, 3.2 and 6.4 Myr, respectively. For each time step, we show the surface velocity (top), the temperature field (middle) and the effective viscosity (bottom). Note that viscosity is normalized by a reference value of $\eta_0 = 10^{20}$ Pa s.

the effective viscosity to between $\sim 10^{18}$ and $\sim 10^{19}$ Pa s. Initially, the slab falls within the upper mantle and with a gap between the base of the slab and the top of the high viscosity lower mantle, the plate velocity increases to just over 70 mm yr^{-1} during a 3.2 Myr time period (Fig. 11b). The slab descends nearly vertically, and since the weak zone for the plate interface does not move, the slab dip increases as the slab descends, and the base of the slab bends as it starts to be affected by the high viscosity lower mantle. During this interaction with the lower mantle, slab descent slows and the subducting plate velocity decreases to about 2–3 cm yr^{-1} at 6.4 Myr (Fig. 11c). The slab has changed from its initial configuration in terms of its dip, depth of penetration, and morphology. This final thermal structure (Fig. 11c) is, together with the surface horizontal velocity, used as data in the inversion.

As in the cylinder sinker model, we first conduct an initial temperature-only inversion assuming that the true viscosity parameters are known. During the inversion, we choose a half-space cooling model as initialization for the initial temperature. In principle, the cooling age can be constructed from surface velocity and the plate tectonic reconstruction. Here, for simplicity, we just use a cooling age consistent with the true initial condition background. Compared to the cylinder sinking problem, the subduction inversion problem is substantially more difficult because of the larger viscosity contrasts near the ridge and trench and the associated mesh refinement there. For example, we computed cases with the LBFGS algorithm without a pre-conditioner, that is, using a scaled identity matrix for R_0 in the LBFGS algorithm. The progress of the inversion was slow, and a line search in the LBFGS algorithm failed before substantial progress in the minimization was made. For the stiffness matrix K-pre-conditioned LBFGS, the inversion greatly improves: the cost function components $\mathcal{J}_S$ and $\mathcal{J}_F$ are reduced by 4 orders of magnitude, indicating that the fit to the data is good; the recovered initial temperature is also near to that of the true model. We then conduct a two parameters inversion, the pre-factor C_1 in the upper 410 km, and the nonlinear exponent n_1 in the upper mantle, while assuming that the initial temperature and other parameters are known. We find convergence to nearly the exact values, as expected from our experience for the cylinder model (Fig. 12a). More inversion results in which a lower mantle pre-factor C_2 is inferred are summarized in Table 2.

Finally, we conduct a joint inversion of $\mathbf{T}_{\text{init}}$, C_1, and n_1, starting from two sets of different guesses. In both cases, the starting guess for the initial temperature is again the half-space cooling model mentioned previously. In the first joint inversion case, we choose a guess of

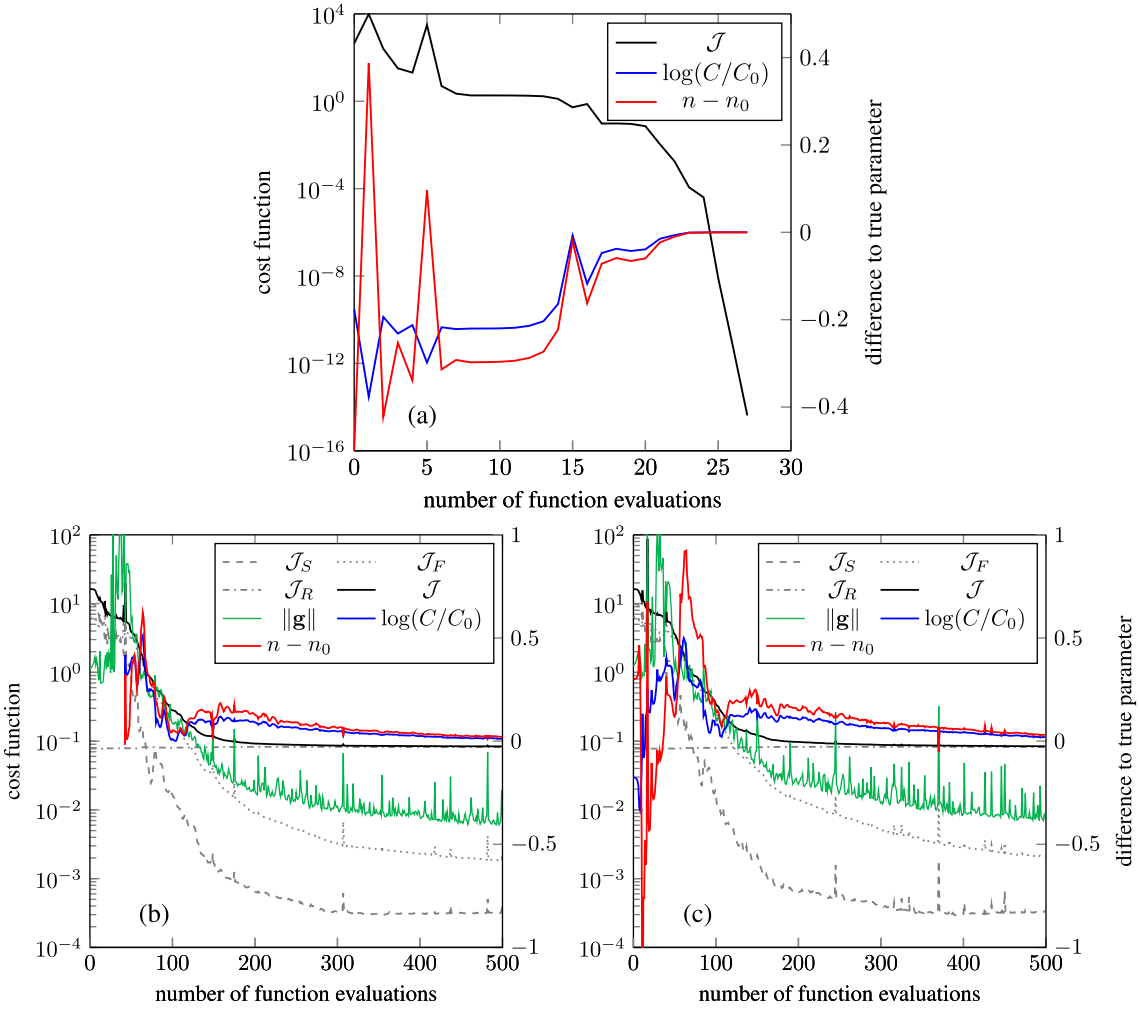

Figure 12. Convergence of inversion in subduction problem. Plotted are the objective and the gradient norms, and iterates for C_1 and n_1 for: (a) Inversion of (C_1, n_1) with initial temperature and other parameters known; (b) Case 1 and (c) Case 2 for joint inversion of $(C_1, n_1, \mathbf{T}_{\text{init}})$.

Table 2. Summary of true, initial and recovered rheology parameters for cylinder sinker and subduction problems.

	Inverting $\mathbf{T}_{\text{init}}$?	Unknown scalar parameters	True values	Initialization values	$\alpha_S, \alpha_F, \alpha_R$	#fvals	Recovered values
	No	C, n (Fig. 7)	1000, 2	500, 2.5	10^3, 10^3, 0	37	1000.0, 2.000
Sinker (Section 8)	Yes	C, n (Fig. 8a)	1000, 2	300, 2.5	10^{-2}, 1, 10^{-5}	220	993.0, 1.996
	Yes	C, n (Fig. 8b)	1000, 2	500, 2.5	10^{-2}, 1, 10^{-5}	280	1416.3, 2.135
	No	C_1, n_1(Fig. 12a)	3e04, 3	2e04, 2.5	10^3, 0, 0	28	3.0e4, 3.0
	No	C_2, n_1	3e04, 3	2e04, 2.5	10, 10^3, 0	24	3.0e04, 3.0
Subd. (Section 9)	No	C_1, C_2, n_1	3e04, 6e04, 3	2e04, 2e04, 2.5	10, 10^3, 0	36	3.0e04, 6.0e04, 3.0
	Yes	C_1, n_1 (Fig. 12b)	3e04, 3	2e04, 2.5	10, 10^3, 0.1	500	3.08e4, 3.02
	Yes	C_1, n_1 (Fig. 12c)	3e04, 3	2e04, 3.3	10, 10^3, 0.1	500	3.14e4, 3.03

$C_1 = 2 \times 10^4$ and $n_1 = 2.5$; in the second case, we choose a guess of $C_1 = 2 \times 10^4$ and $n_1 = 3.3$. For the recovered C_1 and n_1, both cases show good convergence to the true value (Figs 12b and c), although neither exactly reaches the true value as there are small trade-offs and small errors in the recovered initial temperatures (see summary in Table 2).

We show the inversion process of surface velocity, temperature, and viscosity for the first joint inversion case in Fig. 13 (the second case is similar). The initial guess (1st function evaluation) does not fit the surface velocity and final temperature, as indicated by the large values of $\mathcal{J}_S$ and $\mathcal{J}_F$ (Fig. 12b). After 50 function evaluations, the shape of a subducted slab appears within the earlier blurry cool region, while the fit to surface velocity and final temperature improves ($\mathcal{J}_S$ reduces by one order of magnitude, and $\mathcal{J}_F$ reduces by half). Finally, after 500 function evaluations, the fit to the data becomes quite good, and the recovered initial temperature is also near the true model, achieving about 4 orders of magnitude reduction for $\mathcal{J}_S$ and $\mathcal{J}_F$. Indeed, the final recovered initial temperature (Fig. 13e) is visually close to the actual initial

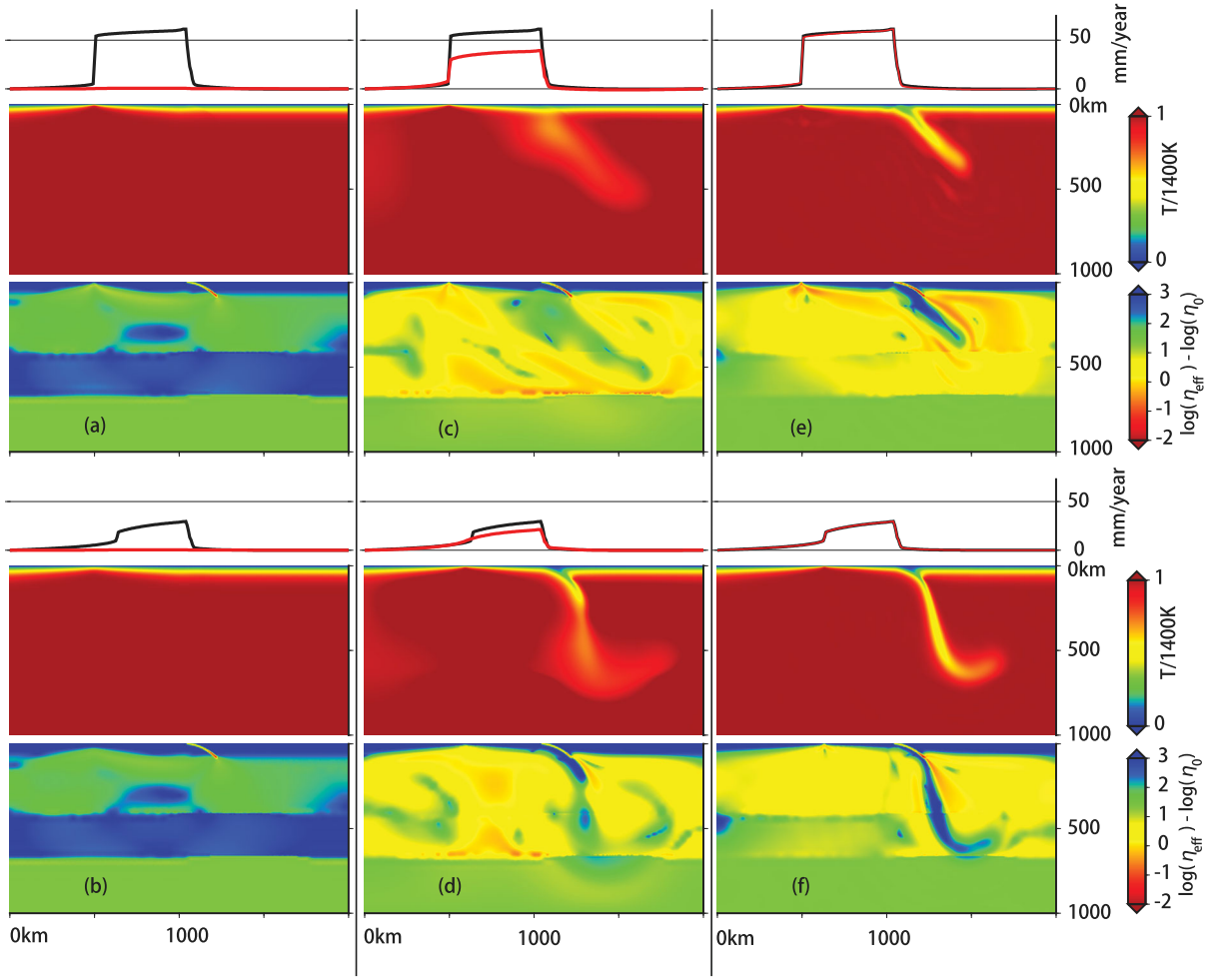

Figure 13. Iterations for (C_1, n_1, $\mathbf{T}_{\text{init}}$)-inversion for subduction problem using the K-pre-conditioned LBFGS method. (a) and (b) correspond to 0 and 50 time step for the first function evaluation. Similarly, (c) and (d) for the 50th function evaluation, and (e) and (f) for the 500th function evaluation. Each panel shows, on the top, the computed surface velocity (red) and the surface velocity data (black); in the middle, the temperature is shown, and the bottom shows the effective viscosity.

temperature (Fig. 13a), except for some high-frequency, but low amplitude differences. However, the quantities which are likely the most important geophysically and geologically—slab dip, depth extent and thermal thickness—are recovered accurately.

10 DISCUSSION AND SUMMARY

For known viscosity parameters in the constitutive relation, our results indicate that the initial condition of our model can be recovered well from final temperature and surface velocity history data. This confirms the finding in Horbach *et al.* (2014), where the authors find that a strong global minimum exists for the initial condition inversion problem. However, in the problem considered here, in contrast to Horbach *et al.* (2014), the effective viscosity is unknown because of the temperature and strain-rate dependence of the viscosity. Assuming the true initial temperature, we demonstrated that the two viscosity parameters (pre-factor in the viscosity law and the nonlinear exponent) can be recovered accurately, even under strong trade-offs that are manifest as a flat valley of the objective function. Our joint inversion of initial temperature and viscosity parameters shows that, while initial condition and effective viscosity can be reasonably recovered, the viscosity parameters themselves may be subject to strong trade-offs due to the ill-conditioning of the inversion problem. Additional study, such as calculation of the Hessian, or using a Bayesian framework that includes prior information would help to further analyse this trade-off, as in Ratnaswamy *et al.* (2015).

In our tests, we have committed the so-called ‘inverse crime’ since we used the same code to generate synthetic observations as for the inversion, while adding no noise to the observations. Thus our tests are mainly used to validate the correctness of our implementation, and to test the performance of the methods for this large-scale PDE-constrained optimization problem. However, the subduction model considered can be extended to circumstances with observational constraints. Burkett & Billen (2009) studied the ridge-trench interaction in Baja California, and recovered subduction and the detachment history of the slab, by computing multiple forward cases that explored the effects of different parameters, including subducted slab length, distance of the ridge from the trench, shear zone strength and yield stress.

It would be helpful to determine the ability to recover these parameters using an adjoint inversion. For example, the inversion may produce an initial temperature condition where subducted slab length and distance of the ridge can be measured directly, and viscosity parameters governing shear zone strength and yield stress are recovered automatically.

The regional subduction problem formulated uses a simple free-slip boundary condition, but the regional dynamics is influenced by this simplification from the free-surface (Crameri *et al.* 2012). However, the topography, including its evolution, is a fundamental constraint on the dynamics (Gurnis *et al.* 2004). A next step as the adjoint inversion is advanced is the incorporation of topography in addition to surface velocities. There are different levels at which this can be achieved in an inverse framework, and some are rather challenging. For instance, computing sensitivities (e.g. through adjoints) of a free surface Stokes flow simulation requires shape derivatives and thus increases the complexity significantly. In instantaneous inverse problems, where it is reasonable to assume that the geometry is in a steady state, a computationally more feasible approach for the inverse problem is possible. We can incorporate a deformed (e.g. present day) geometry into the inverse problem assuming that the component of normal velocity to the surface vanishes (approximately), as a consequence of the stationarity of the geometry.

Additional work is required before the inversion approach described here can be used in large-scale 3-D problems. First, a good initial guess of temperature will accelerate the optimization. Methods such as simple backward advection (Conrad & Gurnis 2003; Ismail-Zadeh *et al.* 2004; Liu & Gurnis 2008) and data assimilation (Bower *et al.* 2015), can potentially provide a better guess than the half-space cooling model we have used here. Second, second-order methods, at least for scalar viscosity parameters (e.g. Ratnaswamy *et al.* 2015), can also speed up the optimization. Finally, there are also several variants of our direct joint inversion to be tested. For example, we may first recover the viscosity parameters using just present-day observations, as in Ratnaswamy *et al.* (2015), then constrain the initial temperature assuming these recovered viscosity parameters remain invariant as the inversion progresses backward in time. One can also envision a stage-wise inversion, as in Ismail-Zadeh *et al.* (2004), where instead of recovering temperature at one distinct point in the past (initial condition) directly, many smaller time-interval inversions are performed that sequentially recover the temperature initial condition. Although not exactly equivalent to the inversion discussed here, these two variants may potentially speed up the recovery. We also envision that convergence of 3-D time-dependent adjoint model computations can be accelerated through a multilevel approach, which uses a hierarchy of temporally and spatially coarsened problems. In such cases, one could use large time steps (and coarser meshes) for most of the computation, and upon convergence of a coarse model, refine both the temporal and spatial resolution.

ACKNOWLEDGEMENTS

DL and MG were supported by the National Science Foundation under EAR-1247022. We would like to thank Mark Simons for comments and suggestions and David May and Alik Ismail-Zadeh for detailed and careful reviews that helped us to significantly improve the manuscript.

REFERENCES

Atwater, T., 1970. Implications of Plate Tectonics for the Cenozoic Tectonic Evolution of Western North America, *Bull. geol. Soc. Am.,* **81**, 3513–3536.

Bangerth, W., Hartmann, R. & Kanschat, G., 2007. deal.II—A general-purpose object-oriented finite element library, *ACM Trans. Math. Softw.,* **33**(4), 24–es.

Baumann, T. & Kaus, B.J., 2015. Geodynamic inversion to constrain the nonlinear rheology of the lithosphere, *Geophys. J. Int.,* **202**(2), 1289–1316.

Billen, M.I., 2008. Modeling the dynamics of subducting slabs, *Annu. Rev. Earth Planet. Sci.,* **36**(1), 325–356.

Billen, M.I. & Hirth, G., 2007. Rheologic controls on slab dynamics, *Geochem. Geophys. Geosyst.,* **8**(8), Q08012, doi:10.1029/2007GC001597.

Blankenbach, B. *et al.*, 1989. A benchmark comparison for mantle convection codes, *Geophys. J. Int.,* **98**(1), 23–38.

Bonito, A., Guermond, J.L. & Popov, B., 2014. Stability analysis of explicit entropy viscosity methods for non-linear scalar conservation equations, *Math. Comput.,* **83**(287), 1039–1062.

Borzì, A. & Schulz, V., 2012. *Computational Optimization of Systems Governed by Partial Differential Equations*, SIAM.

Bower, D.J., Gurnis, M. & Flament, N., 2015. Assimilating lithosphere and slab history in 4-D Earth models, *Physics Earth planet. Inter.,* **238,** 8–22.

Brooks, A.N. & Hughes, T.J.R., 1982. Streamline upwind/Petrov-Galerkin formulations for convection dominated flows with particular emphasis on the incompressible Navier-Stokes equations, *Comput. Methods Appl. Mech. Eng.,* **32**(1–3), 199–259.

Bunge, H.P., Richards, M.A., Lithgow-Bertelloni, C., Baumgardner, J.R., Grand, S.P. & Romanowicz, B.A., 1998. Time scales and heterogeneous structure in geodynamic earth models, *Science,* **280**(5360), 91–95.

Bunge, H.P., Hagelberg, C.R. & Travis, B.J., 2003. Mantle circulation models with variational data assimilation: inferring past mantle flow and structure from plate motion histories and seismic tomography, *Geophys. J. Int.,* **152**(2), 280–301.

Burkett, E.R. & Billen, M.I., 2009. Dynamics and implications of slab detachment due to ridge-trench collision, *J. geophys. Res.,* **114**(12), B12402, doi:10.1029/2009JB006402.

Burstedde, C., Wilcox, L.C. & Ghattas, O., 2011. p4est: scalable algorithms for parallel adaptive mesh refinement on forests of octrees, *SIAM J. Sci. Comput.,* **33**(3), 1103–1133.

Burstedde, C., Stadler, G., Alisic, L., Wilcox, L.C., Tan, E., Gurnis, M. & Ghattas, O., 2013. Large-scale adaptive mantle convection simulation, *Geophys. J. Int.,* **192**(3), 889–906.

Conrad, C.P. & Gurnis, M., 2003. Seismic tomography, surface uplift, and the breakup of Gondwanaland: integrating mantle convection backwards in time, *Geochem. Geophys. Geosys.,* **4**(3), doi:10.1029/2001GC000299.

Crameri, F., Tackley, P.J., Meilick, I., Gerya, T.V. & Kaus, B.J.P., 2012. A free plate surface and weak oceanic crust produc single-sided subduction on Earth, *Geophys. Res. Lett.,* **39**(3), L03306, doi:10.1029/2011GL050046.

Davies, G.F., 1999. *Dynamic Earth: Plates, Plumes and Mantle Convection,* Cambridge Univ. Press.

Garel, F., Goes, S., Davies, D.R., Davies, J.H., Kramer, S.C. & Wilson, C.R., 2014. Interaction of subducted slabs with the mantle transition-zone: a regime diagram from 2-D thermomechanical models with a mobile trench and an overriding plate, *Geochem. Geophys. Geosyst.,* **15**(5), 1739–1765.

Gerya, T., 2011. Future directions in subduction modeling, *J. Geodyn.,* **52**(5), 344–378.

Giles, M.B. & Pierce, N.A., 2000. An introduction to the adjoint approach to design, *Flow Turbulence Combust.,* **65**(3-4), 393–415.
Gunzburger, M.D., 2003. *Perspectives in Flow Control and Optimization,* SIAM.
Gurnis, M., Hall, C. & Lavier, L., 2004. Evolving force balance during incipient subduction, *Geochem. Geophys. Geosyst.,* **5**(7), 1–31.
Horbach, A., Bunge, H.P. & Oeser, J., 2014. The adjoint method in geodynamics: derivation from a general operator formulation and application to the initial condition problem in a high resolution mantle circulation model, *GEM - Int. J. Geomath.,* **5**(2), 163–194.
Hughes, T.J.R., 1987. *The Finite Element Method: Linear Static and Dynamic Finite Element Analysis,* Courier Corporation.
Ismail-Zadeh, A., Schubert, G., Tsepelev, I. & Korotkii, A., 2004. Inverse problem of thermal convection: numerical approach and application to mantle plume restoration, *Phys. Earth planet. Inter.,* **145**(1–4), 99–114.
Kronbichler, M., Heister, T. & Bangerth, W., 2012. High accuracy mantle convection simulation through modern numerical methods, *Geophys. J. Int.,* **191**(1), 12–29.
Lenardic, A., Moresi, L.-N. & Muhlhaus, H., 2003. Longevity and stability of cratonic lithosphere: insights from numerical simulations of coupled mantle convection and continental tectonics, *J. geophys. Res.,* **108**(B6), 1–15.
Liu, L. & Gurnis, M., 2008. Simultaneous inversion of mantle properties and initial conditions using an adjoint of mantle convection, *J. geophys. Res.,* **113**(8), 1–17.
Liu, L., Spasojevic, S. & Gurnis, M., 2008. Reconstructing Farallon plate subduction beneath North America back to the Late Cretaceous, *Science,* **322**(5903), 934–938.
McKenzie, D.P., Roberts, J.M. & Weiss, N.O., 1974. Convection in the earth's mantle: towards a numerical simulation, *J. Fluid Mech.,* **62,** 465–538.
Moresi, L., Gurnis, M. & Zhong, S.J., 2000. Plate tectonics and convection in the Earth's mantle: toward a numerical simulation, *Comput. Sci. Eng.,* **2**(3), 22–33.
Moucha, R. & Forte, A.M., 2011. Changes in African topography driven by mantle convection, *Nat. Geosci.,* **4**(10), 707–712.
Moucha, R., Forte, A.M., Mitrovica, J.X. & Daradich, A., 2007. Lateral variations in mantle rheology: implications for convection related surface observables and inferred viscosity models, *Geophys. J. Int.,* **169**(1), 113–135.
Nocedal, J. & Wright, S., 2006. *Numerical Optimization*, Springer-Verlag.
Ranalli, G. & Karato, S.-I., 1995. *Rheology of the Earth,* vol. 269, Springer Science & Business Media.
Ratnaswamy, V., Stadler, G. & Gurnis, M., 2015. Adjoint-based estimation of plate coupling in a non-linear mantle flow model: theory and examples, *Geophys. J. Int.,* **202**(2), 768–786.
Seton, M. *et al.*, 2012. Global continental and ocean basin reconstructions since 200 Ma, *Earth-Sci. Rev.,* **113**(3–4), 212–270.
Spasojevic, S., Liu, L. & Gurnis, M., 2009. Adjoint models of mantle convection with seismic, plate motion, and stratigraphic constraints: North America since the Late Cretaceous, *Geochem. Geophys. Geosyst.,* **10**(5), Q05W02, doi:10.1029/2008GC002345.
Stadler, G., Gurnis, M., Burstedde, C., Wilcox, L.C., Alisic, L. & Ghattas, O., 2010. The dynamics of plate tectonics and mantle flow: from local to global scales, *Science,* **329**(5995), 1033–1038.
Travis, B.J. *et al.*, 1990. A benchmark comparison of numerical methods for infinite Prandtl number thermal convection in two-dimensional Cartesian geometry, *Geophys. Astrophys. Fluid Dyn.,* **55,** 137–160.
Tröltzsch, F., 2010. *Optimal Control of Partial Differential Equations: Theory, Methods and Applications,* vol. 112 of Graduate Studies in Mathematics, American Mathematical Society.
Worthen, J., Stadler, G., Petra, N., Gurnis, M. & Ghattas, O., 2014. Towards adjoint-based inversion for rheological parameters in nonlinear viscous mantle flow, *Phys. Earth planet. Inter.,* **234,** 23–34.
Yang, T. & Gurnis, M., 2016. Dynamic topography, gravity and the role of lateral viscosity variations from inversion of global mantle flow, *Geophys. J. Int.,* **207,** 1186–1202.
Zhong, S. & Gurnis, M., 1995a. Towards a realistic simulation of plate margins in mantle convection, *Geophys. Res. Lett.,* **22**(8), 981–984.
Zhong, S. & Gurnis, M., 1995b. Mantle convection with plates and mobile, faulted plate margins, *Science,* **267**(5199), 838–843.
Zhong, S., Yuen, D. & Moresi, L., 2007. Numerical methods in mantle convection, *Treatise Geophys.,* **7,** 227–252.

APPENDIX A: DERIVATIONS FOR TERMS IN THE ADJOINT EXPRESSION EQUATIONS (16) AND (17)

Here, we detail derivatives occurring in the adjoint eq. (16) and in the derivative expression eq. (17). Since the matrix $A = A(\mathbf{T}, \mathbf{u}, \mathbf{m})$ depends on the velocity, the components of the derivative of $A\mathbf{u}$ with respect to $\mathbf{u}$ is computed as follows:

$$\left[\frac{\partial A\mathbf{u}}{\partial \mathbf{u}}\right]_{ij} = \frac{\partial A_{ik}\mathbf{u}_k}{\partial \mathbf{u}_j} = A_{ij} + \frac{\partial A_{ik}}{\partial \mathbf{u}_j}\mathbf{u}_k$$
$$= A_{ij} + \int 2\frac{\partial \eta_{\text{eff}}}{\partial \mathbf{u}_j} D(\phi_i^{\boldsymbol{u}}) : D(\boldsymbol{u})\mathrm{d}\Omega,$$

where $\boldsymbol{u}$ is the continuous function corresponding to the coefficient vector $\mathbf{u}$. Because $\eta_{\text{eff}} = \eta_{\min} + \min(\frac{\sigma_{\text{yield}}}{2\sqrt{\varepsilon_{\text{II}}}}, \omega \min(\eta_{\max}, \eta))$, only three cases can occur for η_{eff}, and ignoring the points where the derivative is not unique, we obtain

$$\frac{\partial \eta_{\text{eff}}}{\partial \mathbf{u}_j} = \begin{cases} \dfrac{1-n}{2n}\dfrac{\eta_{\text{eff}} - \eta_{\min}}{\varepsilon_{\text{II}}}\left(D(\boldsymbol{u}) : D(\phi_j^{\boldsymbol{u}})\right), & \eta_{\text{eff}} = \eta_{\min} + \omega\eta, \\ 0, & \eta_{\text{eff}} = \eta_{\min} + \omega\eta_{\max}, \\ -\dfrac{1}{2}\dfrac{\eta_{\text{eff}} - \eta_{\min}}{\varepsilon_{\text{II}}}\left(D(\boldsymbol{u}) : D(\phi_j^{\boldsymbol{u}})\right), & \eta_{\text{eff}} = \eta_{\min} + \dfrac{\sigma_{\text{yield}}}{2\sqrt{\varepsilon_{\text{II}}}}. \end{cases}$$

Next, we focus on the terms $(\frac{\partial A\mathbf{u}}{\partial \mathbf{T}})^{\intercal}\mathbf{v}$, $(\frac{\partial M^S\mathbf{T}}{\partial \mathbf{u}})^{\intercal}\boldsymbol{\lambda}$, $(\frac{\partial C\mathbf{T}}{\partial \mathbf{u}})^{\intercal}\boldsymbol{\lambda}$, $(\frac{\partial C^S\mathbf{T}}{\partial \mathbf{u}})^{\intercal}\boldsymbol{\lambda}$, which occur in the discrete adjoint equation. Let $\boldsymbol{v}$, λ, $\boldsymbol{u}$, T be the continuous function corresponding to discrete $\mathbf{v}$, $\boldsymbol{\lambda}$, $\mathbf{u}$, $\mathbf{T}$, then

$$\left[\left(\frac{\partial A\mathbf{u}}{\partial \mathbf{T}}\right)^{\intercal}\mathbf{v}\right]_k = \mathbf{v}_i\frac{\partial A_{ij}\mathbf{u}_j}{\partial \mathbf{T}_k}$$
$$= \mathbf{v}_i\frac{\partial A_{ij}\mathbf{u}_j}{\partial T}\frac{\partial T}{\mathbf{T}_k}$$

$$= \mathbf{v}_i \frac{\partial \left[\int 2\eta_{\text{eff}} D(\phi_i^{\boldsymbol{u}}) : D(\phi_j^{\boldsymbol{u}}) \mathrm{d}\Omega\right] \mathbf{u}_j}{\partial T} \phi_k^{\text{temp}}$$

$$= \int 2 \frac{\partial \eta_{\text{eff}}}{\partial T} D(\boldsymbol{v}) : D(\boldsymbol{u}) \phi_k^{\text{temp}} \mathrm{d}\Omega,$$

where

$$\frac{\partial \eta_{\text{eff}}}{\partial T} = \begin{cases} -E\omega\eta, & \eta_{\text{eff}} = \eta_{\min}\omega\eta, \\ 0, & \eta_{\text{eff}} = \eta_{\min} + \omega\eta_{\max}, \\ 0, & \eta_{\text{eff}} = \eta_{\min} + \dfrac{\sigma_{\text{yield}}}{2\sqrt{\varepsilon_{\text{II}}}}. \end{cases}$$

Also,

$$\left[\left(\frac{\partial M^S \mathbf{T}}{\partial \mathbf{u}}\right)^{\mathsf{T}} \boldsymbol{\lambda}\right]_k = \boldsymbol{\lambda}_i \frac{\partial M_{ij}^S \mathbf{T}_j}{\partial \mathbf{u}_k}$$

$$= \boldsymbol{\lambda}_i \frac{\partial \left[\int \tau \left(\boldsymbol{u} \cdot \nabla \phi_i^{\text{temp}}\right) \phi_j^{\text{temp}} \mathrm{d}\Omega\right]}{\partial \mathbf{u}_k} \mathbf{T}_j$$

$$= \int \tau \left(\phi_k^{\boldsymbol{u}} \cdot \nabla \lambda\right) T \mathrm{d}\Omega,$$

and

$$\left[\left(\frac{\partial C \mathbf{T}}{\partial \mathbf{u}}\right)^{\mathsf{T}} \boldsymbol{\lambda}\right]_k = \boldsymbol{\lambda}_i \frac{\partial C_{ij} \mathbf{T}_j}{\partial \mathbf{u}_k}$$

$$= \boldsymbol{\lambda}_i \frac{\partial \left[\int \phi_i^{\text{temp}} \boldsymbol{u} \cdot \nabla \phi_j^{\text{temp}} \mathrm{d}\Omega\right]}{\partial \mathbf{u}_k} \mathbf{T}_j$$

$$= \int \lambda \phi_k^{\boldsymbol{u}} \cdot \nabla T \mathrm{d}\Omega.$$

Moreover,

$$\left[\left(\frac{\partial C^S \mathbf{T}}{\partial \mathbf{u}}\right)^{\mathsf{T}} \boldsymbol{\lambda}\right]_k = \boldsymbol{\lambda}_i \frac{\partial C_{ij}^S \mathbf{T}_j}{\partial \mathbf{u}_k}$$

$$= \boldsymbol{\lambda}_i \frac{\partial \left[\left(\tau \boldsymbol{u} \cdot \nabla \phi_i^{\text{temp}}\right) \left(\boldsymbol{u} \cdot \nabla \phi_j^{\text{temp}}\right)\right]}{\partial \mathbf{u}_k} \mathbf{T}_j$$

$$= \int \tau \left(\lambda \phi_k^{\boldsymbol{u}} \cdot \nabla T + T \phi_k^{\boldsymbol{u}} \cdot \nabla \lambda\right) \mathrm{d}\Omega.$$

For the derivatives $\frac{\partial A}{\partial m}$ for C, E, n, we find

$$\left[\begin{array}{ccc} \frac{\partial \eta_{\text{eff}}}{\partial C} & \frac{\partial \eta_{\text{eff}}}{\partial E} & \frac{\partial \eta_{\text{eff}}}{\partial n} \end{array}\right] = \begin{cases} \left[\omega \dfrac{\eta}{C},\ (0.5 - T)\omega\eta,\ -\dfrac{\ln \epsilon_{\text{II}}}{2n^2}\omega\eta\right], & \eta_{\text{eff}} = \eta_{\min} + \omega\eta, \\ 0, & \eta_{\text{eff}} = \eta_{\min} + \omega\eta_{\max}, \\ 0, & \eta_{\text{eff}} = \eta_{\min} + \dfrac{\sigma_{\text{yield}}}{2\sqrt{\varepsilon_{\text{II}}}}, \end{cases}$$

and for $m = \ln C$, or equivalently $C = e^m$

$$\frac{\partial \eta_{\text{eff}}}{\partial m} = \frac{\partial \eta_{\text{eff}}}{\partial C} \frac{\partial C}{\partial m} = \frac{\partial \eta_{\text{eff}}}{\partial C} C,$$

and finally

$$\left(\frac{\partial A}{\partial m}\right)_{ij} = \int 2 \frac{\partial \eta_{\text{eff}}}{\partial m} D(\phi_i^{\boldsymbol{u}}) : D\left(\phi_j^{\boldsymbol{u}}\right) \mathrm{d}\Omega.$$